Robust topology and discrete fiber orientation optimization under principal material uncertainty

Konstantinos-Iason Ypsilantis[a], Matthias G.R. Faes[b], Nikos D. Lagaros[c], Niels Aage[d] and David Moens[a,*,1]

[a] KU Leuven, Department of Mechanical Engineering, Div. LMSD, Jan De Nayerlaan 5, 2860, Sint-Katelijne-Waver , Belgium
[b] TU Dortmund University, Chair for Reliability Engineering, Leonard-Euler-Straße 5, 44227 Dortmund, Germany
[c] National Technical University of Athens, Department of Structural Engineering, Institute of Structural Analysis & Antiseismic Research, School of Civil Engineering, Heroon Polytechniou Str. 9, Zografou Campus, GR-15780 Athens, Greece
[d] Technical University of Denmark, Department of Mechanical Engineering, Koppels Allé, B.404, 2800 Kgs. Lyngby, Denmark

ARTICLE INFO

Keywords:
· Topology Optimization
· Discrete Fiber Orientation Optimization
· Robust Compliance Minimization
· Principal Material Uncertainty
· Material Parameterization Scheme
· Stochastic Finite Element Analysis

Abstract

This paper introduces a formulation of the robust topology optimization problem that is tailored for designing fiber-reinforced composite structures with spatially varying principal mechanical properties. Specifically, a methodology is developed that incorporates the spatial variability in the engineering constants of the composite lamina into the concurrent topology (i.e., material distribution) and morphology (i.e., fiber orientation distribution) optimization problem for the minimization of the robust compliance function. The spatial variability in the mechanical properties of the lamina is modeled as a homogeneous random field within the design domain by means of the Karhunen-Loéve series expansion, and is thereafter intrusively propagated into the stochastic finite element analysis of the composite structure. To carry out the stochastic finite element analysis per iteration of the optimization cycle, the first-order perturbation method is utilized for approximating the current state variables of the physical system. The resulting robust topology and fiber orientation optimization problem is formulated step-by-step for the minimization of the robust compliance function. With the view of solving the optimization problem at hand by means of gradient-based solution algorithms, the first-order derivatives of the involved design functions *w.r.t.* the associated design variables are analytically derived. The present work concludes with a series of numerical examples, focusing on the benchmark academic case studies of the 2D cantilever and the half part of the Messerschmitt-Bölkow-Blohm beam, aiming to demonstrate the developed methodology as well as to explore the effect that different parameterization instances of the random field bear on the predicted topology and morphology of the beams.

1. Introduction

Fiber-Reinforced Composites (FRCs) have become increasingly popular across industrial applications that require lightweight materials of high specific properties. Unlike traditional materials, FRCs allow for the customization of the material's anisotropy to meet the structural requirements. The recent advent of Additive Manufacturing (AM) techniques has greatly facilitated the manufacturing of complex-shaped FRCs at reduced costs and time. Yet, the layer-by-layer printing strategy employed by most AM techniques limits the fiber deposition to being parallel to the printing plane, thereby rendering the design for optimal fiber orientation to be primarily approached as a 2D problem.

Designing for the optimal fiber orientation at the Finite Element (FE) level can be performed by employing either the Continuous Fiber Orientation Optimization (CFOO) or the Discrete Fiber Orientation Optimization (DFOO) scheme. With regard to the former case, the optimal fiber orientation is sought for the FE within the $[0, 180]^\circ$ interval. Foundational contributions in CFOO include the stress-based method, proposed by Cheng et al. [1], and the strain-based method proposed by Pedersen [2, 3, 4]. The rationale of both methods is to align the fiber orientation with the major principal stress/strain trajectories during the optimization cycle in order to maximize the normal stress supported by the fiber. Comparative studies between the two methods carried out by Olhoff et al. [5] and Cheng et al. [1], concluded that the stress-based approach is slightly more efficient than the strain-based method, mainly due to the lower sensitivity the stress field exhibits *w.r.t* variations in the fiber orientation. Conversely, the DFOO scheme

david.moens@kuleuven.be (David Moens)
ORCID(s):

seeks to identify the optimal fiber orientation for the FE from a predefined set of candidates. This set is composed of various effective elasticity tensors of the composite lamina, with each tensor corresponding to a specific candidate fiber orientation, and to interpolate these within the FE domain, DFOO employs a parameterization scheme. Different methods for performing this parameterization have been proposed in the literature. The state-of-the-art includes the Discrete Material Optimization (DMO) proposed in [6], the Shape Functions with Penalization (SFP) proposed in [7, 8], the Bi-value Coding Parameterization (BCP) proposed in [9] and, the more recent Normal Distribution Fiber Optimization (NDFO) technique proposed in [10]. As this work centers around DFOO, the aforementioned techniques are discussed separately in the subsequent sections of the article.

Given that the aforementioned techniques operate at the FE level, they do not guarantee spatial continuity in the fiber orientation distribution within the structural domain. Hence, they might deliver solutions that are not physically attainable. Therefore, to achieve smooth continuous fiber paths within the structure, an alternative approach has been adopted. Herein, a global level set function is defined over the design domain, where the corresponding iso-contours represent the fiber paths. The format of the level set function follows that of the general linear regression model; that is, a set of smooth basis functions is defined over the structural domain and their corresponding weights constitute the design variables of the morphology optimization problem. At every iteration of the optimization cycle, the fiber orientation at a specific location inside the domain is obtained via computing the gradient of the level set function at that location. The current fiber orientation is then utilized to update the local mechanical properties of the domain and conduct next the sensitivity analysis. The optimization progresses until the imposed convergence criterion is met. At the end of the optimization cycle, the final weights of the level-set are derived and its iso-contours are used to represent the optimal fiber paths. Fernandez et al. [11] utilized cubic B-splines as basis functions and incorporated into the corresponding morphology optimization problem the manufacturing constraints associated with the Direct Ink Writing (DIW) printing process. A similar study was conducted by Tian et al. [12] employing fifth-order radial basis functions to parameterize the level set function. In the formulation of the morphology optimization problem, the authors imposed the "offset" constraint on the gradient of the level set function to ensure that its contours (i.e. fiber paths) do not overlap. In a previous study [13], the authors utilized the inverse distance weighting function as the basis function and included the local curvature of the fiber path as an additional constraint in the optimization problem.

Topology Optimization (TO)[14] seeks to identify the optimal density field distribution within the structural domain under specific structural conditions. Numerous methods have been proposed in the literature for the formulation of the Topology Optimization Problem (TOP) for homogeneous structures, the Solid Isotropic Material with Penalization (SIMP) [15, 16] and the Level-Set Method (LSM) [17, 18, 19, 20] being the most popular among them. A summary of all these methods, along with the codes that solve the respective TOP formulations is provided in [21]. To design structures that are optimal in both their morphology and topology, different approaches have been proposed in the literature combining the two individual optimization problems. Nomura et al. [22] proposed the vector parameterization approach that simultaneously optimizes the density field (represented as the magnitude of the vector) and the fiber orientation (represented as the vector orientation). Jiang et al. [23] proposed a framework for concurrently optimizing the topology and morphology of the structure at the FE level, separating —as opposed to the work of Nomura et al. [22]— the design variables of the two optimization problems. In the same work, the authors also examined the effect of the printing plane on the topology and morphology of the final design. The work of Schmidt et al. [24] focused in a similar direction, where the authors proposed a framework for the concurrent Topology and Fiber Orientation Optimization (TFOO) that utilizes the spherical coordinates notation to characterize the fiber orientation within the design domain, as opposed to the earlier work of Jiang et al. [23] where the authors utilized the Cartesian coordinates notation for this purpose.

All studies discussed thus far have been developed under deterministic assumptions holding for the structure; this means that the final designs perform optimally only when subjected to the specific (e.g. nominal) values of the structural conditions they have been optimized for (e.g., loading, boundary conditions, material properties, etc.) and are highly likely to be sensitive to any deviations from these values. In real-world applications, however, the structural conditions are non-deterministic, and it becomes crucial to incorporate these uncertainties into the optimization procedure to ensure that the final design will perform adequately across their entire range, i.e. ensure that the final design is robust. Robust Topology Optimization (RTO) incorporates these uncertainties into the topology optimization procedure to ensure that the topologically optimal design can withstand any realizations of these uncertainties. The majority of the methodologies proposed in the literature on RTO focus on attaining robust homogeneous structures under loading uncertainties. Guest et al. [25] utilized the perturbation method to solve problems under uncertain loads and nodal locations that are characterized by small uncertainties. Zhao et al. [26] formulated a methodology for the minimization

of the robust compliance function utilizing the Karhunen-Loéve (K-L) series expansion to represent the loading uncertainty as a homogeneous Random Field (RF). An extension of this method was recently proposed by Gao et al. [27] where the authors represented the loading uncertainty as an imprecise RF, whereby the two statistical moments of the RF are no longer constant values but are defined within intervals. Other notable contributions to the field of RTO concerning homogeneous structures involve that of Lazarov et al. [28], where the spatial material and geometric uncertainty are represented as homogeneous RFs and are incorporated into the topology optimization procedure, and the work of da Silva et al. [29], where the authors presented a complete mathematical framework for designing topologically robust homogeneous structures when considering the spatial variability in the Young's Modulus. In the latter study, the authors also conducted a series of parametric studies aiming to investigate the effect of the correlation length on the final robust designs. The few studies on RTO for fiber-reinforced composites concentrate also on loading uncertainty. Xu et al. [30] formulated the robust Topology and Fiber Orientation Optimization Problem (TFOOP) when considering the uncertainty in the magnitude and the direction of the loading. In their work, the authors employed the DMO interpolation scheme to optimize the fiber orientation, constraining that way the optimal fiber orientation to lie within the set of candidates. Similar work was conducted by Sheng et al. [31] considering the same type of loading uncertainty. However, in their work, the authors employed the CFOO scheme, thereby allowing the fiber orientation to be freely optimized within the $[0, 180]^\circ$ interval. In addition, to reduce the computational cost of the robust TFOOP, they incorporated the Kriging surrogate model into the devised mathematical framework to conduct the sensitivity analysis for the robust compliance function.

The present work is motivated by the work of da Silva et al. [29]. It focuses, however, on fiber-reinforced composite structures. Specifically, a methodology is proposed that incorporates the spatial variability in the principal material properties of the composite lamina into the robust TFOOP so as to predict topologically and morphologically robust composite structures. The methodology optimizes separately the morphology and topology of the structural domain at the FE level. For topology optimization, the density-based SIMP technique is utilized, while any of the aforementioned techniques from the DFOO scheme can be employed for optimizing the morphology. Concerning the spatial variability in the principal material properties, the methodology is formulated around the assumption that the E_1 Young's Modulus of the composite lamina is stochastic. Based on this premise, the E_1 Young's Modulus is modeled as homogeneous RF within the structural domain and is integrated into the Stochastic Finite Element Analysis (SFEA) that is performed per optimization iteration (see [32], [33]). Finally, the corresponding Topology and Discrete Fiber Orientation Optimization Problem (TDFOOP) is formulated step-by-step for the minimization of the robust compliance function.

The remaining part of this study is organized as follows: As the developed methodology relies on the existing mathematical framework of deterministic Topology and Discrete Fiber Orientation Optimization (TDFOO), to ensure comprehensiveness, an overview of the specific optimization problem is provided in Sec. (2). Subsequently, the formulation of the robust TDFOOP under principal material uncertainty is carried out in two successive parts. The first part, covered in Sec. (3), outlines the process of intrusively incorporating the spatial material variability into the SFEA nested within the optimization cycle. Additionally, the formulation of the SFEA is analytically conducted using the first-order Perturbation-Taylor series expansion method to approximate the current state variables. The second part, covered in Sec. (4), establishes the robust TDFOOP for minimizing the robust compliance function and performs the sensitivity analysis for the involved design functions. To demonstrate the developed methodology and assess the impact of different material variability parameterizations on the final robust designs, numerical examples are presented in Sec. (5). Lastly, the paper concludes in Sec. (6), where the authors present potential extensions, modifications, and discuss areas for further improvement of the proposed methodology.

2. Deterministic Topology and Discrete Fiber Orientation Optimization

This section summarizes the steps involved in formulating the elasticity tensor for the (e) FE in the structural domain for the deterministic TDFOOP. In the authors' view, it is convenient to first revisit the mathematical framework of the deterministic TDFOOP prior to proceeding to its stochastic formulation, as it establishes the necessary groundwork for formulating the latter. The current section is structured as follows: Sec. (2.1) provides an overview of the conventional Discrete Fiber Orientation Optimization Problem (DFOOP), and lists the thus far state-of-the-art techniques for parametrizing the mechanical properties of the candidates within the FE domain. Next, in Sec. (2.2), the DFOOP is combined with the TOP to derive the mathematical expression for the FE's elasticity tensor.

2.1. Discrete Fiber Orientation Optimization

Discrete material optimization seeks to identify the most suitable material for a given design domain from a predefined list of candidate materials. The candidate materials are indirectly represented on this list via their mechanical properties, and an interpolation scheme is employed to parameterize those within the domain of interest. In the case where each FE in the domain constitutes a separate domain of interest, the parameterization scheme reads as follows:

$$\left[C_{e(\xi_e)}\right] = N_{e1(\xi_e)} \cdot \left[C_1\right] + \cdots + N_{en_c(\xi_e)} \cdot \left[C_{n_c}\right] = \sum_{i=1}^{n_c} N_{ei(\xi_e)} \cdot \left[C_i\right] \quad \ldots \quad e = 1 : n_e, \tag{1}$$

$$\text{s.t.} \quad \sum_{i=1}^{n_c} N_{ei(\xi_e)} = 1, \tag{2}$$

where the subscript (e) enumerates the FE after discretizing the structural domain into n_e FEs, n_c is the number of candidate materials assigned to it, $\left[C_i\right]$ is the elasticity tensor representing the $\left(i^{th}\right)$ in order candidate material, and $N_{ei} \in \left[0, 1\right]$ the weight assigned to it, expressed as an explicit function of the so-called material design variable vector $\boldsymbol{\xi}_e$. The objective of the Material Optimization Problem (MOP) is to solve for each $\boldsymbol{\xi}_e$ design variable vector by optimizing the performance metric function. At the end of the optimization cycle, a unique material must be identified from the list for the FE, and to enforce this requirement, each FE is subject to the constraint of Eq. (2).

In the context of discrete fiber orientation optimization, the candidate materials are the different effective mechanical properties of the lamina, each tied to a distinct candidate fiber orientation. The effective mechanical property corresponding to the θ_i candidate fiber orientation is computed by passing the principal elasticity tensor of the lamina through the following second-order transformation:

$$\left[C_i\right] = \left[T_i\right] \cdot \left[C_p\right] \cdot \left[T_i\right]^T \quad \ldots \quad i = 1 : n_c, \tag{3}$$

where $\left[T_i\right]$ is the transformation matrix associated with the θ_i candidate fiber orientation and $\left[C_p\right]$ is the in-plane elasticity tensor corresponding to the principal coordinate system of the lamina. Considering the 2D case, the $\left[T_i\right]$ and $\left[C_p\right]$ matrices are defined as follows:

$$\left[T_i\right] = \begin{bmatrix} \cos^2(\theta_i) & \sin^2(\theta_i) & -2 \cdot \cos(\theta_i) \cdot \sin(\theta_i) \\ \sin^2(\theta_i) & \cos^2(\theta_i) & 2 \cdot \cos(\theta_i) \cdot \sin(\theta_i) \\ \cos(\theta_i) \cdot \sin(\theta_i) & -\cos(\theta_i) \cdot \sin(\theta_i) & \cos^2(\theta_i) - \sin^2(\theta_i) \end{bmatrix}, \quad \left[C_p\right] = \begin{bmatrix} \frac{1}{E_1} & -\frac{\upsilon_{12}}{E_1} & 0 \\ -\frac{\upsilon_{12}}{E_1} & \frac{1}{E_2} & 0 \\ 0 & 0 & \frac{1}{G_{12}} \end{bmatrix}^{-1}, \tag{4}$$

where $E_1,\ E_2$ are the Young's moduli along the major and minor axis of the lamina, respectively, and $G_{12},\ \upsilon_{12}$ are the in-plane shear modulus and Poisson's ratio, respectively.

To perform the interpolation of Eq. (1), different techniques can be employed from the literature. Table 1 lists the weight functions proposed in the literature for the conventional discrete fiber orientation optimization. In the mathematical expression of the weight functions, the semicolon indicates that $p_\theta \in \mathbb{R}^+$ is a design parameter specific to each technique, and for all techniques serves the purpose of shifting the intermediate values of the penalized quantity toward its discrete binary values, so as to ensure that a unique material is identified for the FE at the end of the optimization.

2.2. Formulation of the FE's elasticity tensor for the deterministic TDFOO

The density-based topology optimization is combined with discrete fiber orientation optimization by multiplying the parameterized mechanical property of Eq. (1) with the true relative density $x_e \in \left[x_{e_{min}}, 1\right]$ of the FE, where $x_{e_{min}}$ a very small positive value. To achieve smoothness in both the morphology and topology distribution of the final design, filters are applied to the crude design variables of each individual optimization problem. More specifically, smoothing in the topology of the domain is achieved by passing the relative densities through the following filter:

Method	Weight $N_{ei(\xi_e;p_\theta)}$	Bounds
DMO4 [6]	$\xi_{ei}^{p_\theta} \cdot \prod_{\substack{j=1 \\ j\neq i}}^{n_c} \left(1-\left(\xi_{ej}\right)^{p_\theta}\right)$	$\boldsymbol{\xi_e} \in [0,1]^{n_c}$
DMO5 [6]	$\frac{\hat{w}_{ei}}{\sum_{i=1}^{n_c} \hat{w}_{ei}}$ with $\hat{w}_{ei} = \xi_{ei}^{p_\theta} \cdot \prod_{\substack{j=1 \\ j\neq i}}^{n_c} \left(1-\left(\xi_{ej}\right)^{p_\theta}\right)$	$\boldsymbol{\xi_e} \in [0,1]^{n_c}$
SFP [7, 8]	$\left(\frac{1}{4} \cdot \prod_{j=1}^{2} \left(1+\xi_{ej}\cdot\xi_{ij}\right)\right)^{p_\theta}, \quad i = 1:4$	$\boldsymbol{\xi_e} \in [-1,1]^2$
BCP [9]	$\left(\frac{1}{2^k} \cdot \prod_{j=1}^{k} \left(1+\xi_{ej}\cdot\xi_{ij}\right)\right)^{p_\theta}, \quad k = \lceil \log_2 n_c \rceil$	$\boldsymbol{\xi_e} \in [-1,1]^{\lceil \log_2 n_c \rceil}$
	where $\xi_{ij} = \begin{cases} 1 & i \in [1,\ 2^{j-1}] \\ -1 & i \in [2^{j-1},\ 2^j] \\ \xi_{mj} & m \in [2^j+1,\ 2^k] \quad \text{where} \quad m = 2^{\lceil \log_2 i \rceil} + 1 - i \end{cases}$	
NDFO [10]	$\frac{\hat{w}_{ei}}{\sum_{i=1}^{n_c} \hat{w}_{ei}}$ with $\hat{w}_{ei} = e^{-\frac{(\xi_e - i)^2}{2\cdot p_\theta^2}}$	$1 \leq \xi_e \leq n_c$

Table 1
The weight function associated with each material interpolation technique proposed in the literature.

$$\tilde{x}_e = \frac{\sum_{j_e \in \mathbb{N}_e} \left(1 - \frac{\|\boldsymbol{x}_c^{j_e} - \boldsymbol{x}_c^e\|}{R}\right) \cdot x_{j_e}}{\sum_{j_e \in \mathbb{N}_e} \left(1 - \frac{\|\boldsymbol{x}_c^{j_e} - \boldsymbol{x}_c^e\|}{R}\right)} \quad \ldots \quad e = 1:n_e, \quad \boldsymbol{x}_c^{j_e} \in \Omega_e, \tag{5}$$

where $\tilde{x}_e$ is the physical relative density of the (e) FE, $\left(j_e\right)$ is its neighboring FE of true relative density x_{j_e} with its centroid $\boldsymbol{x}_c^{j_e}$ located within the filter radius R that counts from the centroid $\boldsymbol{x}_c^e$ of (e), and $\mathbb{N}_e$ is the set of FEs within the neighborhood of (e). Denoting, for the sake of brevity, the ratio of the centroidal distance between two neighbor FEs to the filter radius as $\bar{d}_{j_e e}$, Eq. (5) is simplified as follows:

$$\tilde{x}_e = \frac{\sum_{j_e \in \mathbb{N}_e} \left(1 - \bar{d}_{j_e e}\right) \cdot x_{j_e}}{\sum_{j_e \in \mathbb{N}_e} \left(1 - \bar{d}_{j_e e}\right)}. \tag{6}$$

To enforce intermediate values of the physical relative densities towards the 0/1 bounds, they are either penalized by a parameter $p \in \mathbb{R}_{\geq 1}$ or pass through a dynamic Heaviside-type transformation [34]. For the sake of simplicity throughout the development of the methodology in the upcoming sections, the former projection approach is adopted in this work.

To smooth the morphology of the structural domain, the above filtering process is repeated for each individual component i of the FE's weight functions. To account, however, for the fact that the topology, and thereby the

morphology, of the void FEs do not contribute to the overall stiffness of the structural domain, the filter for the weight functions is designed to suppress the impact of the near-void FEs' morphology throughout the filtering process of the domain's morphology [35]:

$$\tilde{N}_{ei} = \frac{\sum_{j_e \in \mathbb{N}_e} \left(1 - \bar{d}_{j_e e}\right) \cdot N_{j_e i(\xi_{j_e})} \cdot \tilde{x}^p_{j_e}}{\sum_{j_e \in \mathbb{N}_e} \left(1 - \bar{d}_{j_e e}\right) \cdot \tilde{x}^p_{j_e}}. \tag{7}$$

Hence, by including the physical relative densities of the neighboring FEs in the filtering process of the weight functions, it is ensured that the morphology of each FE (e) is primarily impacted by the morphology of its non-void neighboring FEs. Similar to the physical relative densities, to enforce intermediate values of each weight function towards its 0/1 bounds, it is either penalized by a parameter $p_n \in \mathbb{R}_{\geq 1}$ or undergoes a dynamic Heaviside-type transformation. Again, for simplicity purposes, the former projection approach is adopted for the weight functions.

Finally, the elasticity tensor of the (e) FE for the deterministic TDFOOP is expressed in terms of the physical design variables $\tilde{x}_e$ and $\tilde{N}_{ei}$ as follows:

$$\left[C_{e(\tilde{x}_e, \tilde{\boldsymbol{N}}_e)}\right] = \tilde{x}^p_e \cdot \left(\sum_{i=1}^{n_c} \tilde{N}^{p_n}_{ei} \cdot [C_i]\right) \quad \ldots \quad e = 1 : n_e, \tag{8}$$
$$\text{s.t.} \quad \sum_{i=1}^{n_c} \tilde{N}^{p_n}_{ei} - 1 = 0,$$

where the bold symbol notation is utilized in Eq. (8) to represent the physical weight functions of the FE in a vector format. It is emphasized that both the physical relative density and weight functions of the FE form explicit functions of the true relative densities of its neighboring FEs. Moreover, the physical weight functions are explicit functions of the orientation variable vector of its neighboring FEs $\boldsymbol{\xi}_{j_e}$. Although these dependencies are important to bear in mind, they have been omitted in Eq. (8) for notational brevity.

3. Robust TDFOO- Pt. I: Incorporation of the principal material variability into the SFEA

In this section, the spatial variability in the engineering constants of the composite lamina is incorporated into the nested SFEA that is performed at each iteration of the robust TDFOO loop. The current section is structured as follows: in Sec. (3.1), the Young's modulus along the major axis of the composite lamina is assumed to be stochastic and is modeled as a homogeneous RF within the composite domain. As a result, the originally deterministic principal elasticity tensor of Eq. (4) becomes itself stochastic which, in the framework of the FE-based DFOO, after undergoing the respective in-plane transformations of Eq. (3) generates a set of candidate stochastic effective elasticity tensors for the FE. Sec. (3.2) formulates the SFEA that is carried out at each iteration of the robust TDFOO loop to compute the current state vectors of the physical system. As the states of the physical system are conditioned on its current topology and morphology, a different state is realized per iteration of the optimization loop. For this reason, the SFEA is formulated in this section assuming that we are found at a specific iteration n (or design point) inside the optimization cycle, where a particular morphology and topology have already been realized for the structural domain.

3.1. Formulation of the FE's elasticity tensor for the robust TDFOO

To formulate the mathematical framework of the methodology, the spatial variability is assumed in the E_1 Young's Modulus along the major axis of the composite lamina. The reasoning behind this assumption stems from that the mechanical performance of composite structures —especially 3D printed structures— is primarily dictated by the properties of the fiber, and thereby, variations in E_1 may have a much more substantial effect on the overall structural response compared to those in E_2 or G_{12}. Based on this premise, the variability in E_1 is modeled as a homogeneous RF within the structural domain and is denoted as $E_1 \sim \mathcal{GP}\left(\mu_{E_1}, \sigma^2_{E_1}\right)$, where μ_{E_1} and $\sigma^2_{E_1}$ represent the constant true mean and variance of the field, respectively. Concerning the representation of the RF within the structural domain, various discretization techniques can be utilized for this purpose. Among these, the midpoint technique [36] is preferred in this study primarily due to its simplicity, wherein the RF is represented at the centroid $\boldsymbol{x}^e_c$ of each FE (e). Thus, employing the K-L series expansion technique to model the RF reads as follows:

$$\widehat{X}_{1(\boldsymbol{x}_c^e,\boldsymbol{z})} = \mu_{E_1} + \sum_{m=1}^{M} \sqrt{\lambda_m} \cdot \phi_{m(\boldsymbol{x}_c^e)} \cdot z_m, \qquad \text{where} \quad z_m \sim \mathcal{N}(0,1), \tag{9}$$

where $\widehat{X}_{1(\boldsymbol{x}_c^e,\boldsymbol{z})}$ is the approximation of the E_1 stochastic property at the centroid $\boldsymbol{x}_c^e$ of the (e) FE. After decomposing the covariance matrix, which contains the spatial correlation of the stochastic property at the FE centroids scaled by the variance of the RF, the stochastic property is represented by a finite series of M stochastic variables. The stochastic variables $z_{m=1:M}$ follow the standard normal distribution and are independent, i.e. $\mathbb{E}\left[z_l \cdot z_k\right] = \delta_{lk}$, where δ_{lk} the Kronecker delta function. Lastly, λ_m and $\phi_{m(\boldsymbol{x}_c^e)}$ are the eigenvalues and corresponding orthogonal eigenfunctions derived after decomposing the covariance matrix.

Substituting in Eq. (4), the deterministic E_1 Young's Modulus with its stochastic formulation in Eq. (9), the principal elasticity tensor reads as follows:

$$[C_{p(\boldsymbol{x}_c^e,\boldsymbol{z})}] = [S_{p(\boldsymbol{x}_c^e,\boldsymbol{z})}]^{-1} = \begin{bmatrix} \frac{1}{\widehat{X}_{1(\boldsymbol{x}_c^e,\boldsymbol{z})}} & \frac{-\upsilon_{21}}{E_2} & 0 \\ \frac{-\upsilon_{12}}{\widehat{X}_{1(\boldsymbol{x}_c^e,\boldsymbol{z})}} & \frac{1}{E_2} & 0 \\ 0 & 0 & \frac{1}{G_{12}} \end{bmatrix}^{-1} = \begin{bmatrix} -\frac{\widehat{X}_{1(\boldsymbol{x}_c^e,\boldsymbol{z})}}{\upsilon_{12}\cdot\upsilon_{21}-1} & -\frac{E_2\cdot\upsilon_{12}}{2\cdot(\upsilon_{12}\cdot\upsilon_{21}-1)} - \frac{\widehat{X}_{1(\boldsymbol{x}_c^e,\boldsymbol{z})}\cdot\upsilon_{21}}{2\cdot(\upsilon_{12}\cdot\upsilon_{21}-1)} & 0 \\ -\frac{E_2\cdot\upsilon_{12}}{2\cdot(\upsilon_{12}\cdot\upsilon_{21}-1)} - \frac{\widehat{X}_{1(\boldsymbol{x}_c^e,\boldsymbol{z})}\cdot\upsilon_{21}}{2\cdot(\upsilon_{12}\cdot\upsilon_{21}-1)} & -\frac{E_2}{(\upsilon_{12}\cdot\upsilon_{21}-1)} & 0 \\ 0 & 0 & G_{12} \end{bmatrix} \tag{10}$$

From Eq. (10), it is observed that only some of the tensor's entries contain the RF while others remain constant terms. Applying the transformation of Eq. (3) to the stochastic principal elasticity tensor for any candidate fiber orientation $\theta_i \in (-90,0)^\circ \cup (0,90)^\circ$, the resulting stochastic effective elasticity tensor $\left[C_{i(\boldsymbol{x}_c^e,\boldsymbol{z})}\right]$ can be expressed into the following format:

$$\left[C_{i(\boldsymbol{x}_c^e,\boldsymbol{z})}\right] = \begin{bmatrix} a_{11}\cdot\widehat{X}_{1(\boldsymbol{x}_c^e,\boldsymbol{z})} + b_{11} & a_{12}\cdot\widehat{X}_{1(\boldsymbol{x}_c^e,\boldsymbol{z})} + b_{12} & a_{13}\cdot\widehat{X}_{1(\boldsymbol{x}_c^e,\boldsymbol{z})} + b_{13} \\ a_{21}\cdot\widehat{X}_{1(\boldsymbol{x}_c^e,\boldsymbol{z})} + b_{21} & a_{22}\cdot\widehat{X}_{1(\boldsymbol{x}_c^e,\boldsymbol{z})} + b_{22} & a_{23}\cdot\widehat{X}_{1(\boldsymbol{x}_c^e,\boldsymbol{z})} + b_{23} \\ a_{31}\cdot\widehat{X}_{1(\boldsymbol{x}_c^e,\boldsymbol{z})} + b_{31} & a_{32}\cdot\widehat{X}_{1(\boldsymbol{x}_c^e,\boldsymbol{z})} + b_{32} & a_{33}\cdot\widehat{X}_{1(\boldsymbol{x}_c^e,\boldsymbol{z})} + b_{33} \end{bmatrix} \tag{11}$$

where a_{ij} and b_{ij}, with (i,j) =1:3, are constant terms arising from the transformation of Eq. (3). It is noted that the above format can be reached for the $\{-90^\circ, 0^\circ, 90^\circ\}$ angles as well by adding (or subtracting, alternatively) to their values some small term $\tau > 0$. Expanding the RF at each entry of the tensor according to Eq. (9), the tensor is decomposed as follows:

$$\left[C_{i(\boldsymbol{x}_c^e,\boldsymbol{z})}\right] = \underbrace{\begin{bmatrix} a_{11}\cdot\mu_{E_1} + b_{11} & a_{12}\cdot\mu_{E_1} + b_{12} & a_{13}\cdot\mu_{E_1} + b_{13} \\ a_{21}\cdot\mu_{E_1} + b_{21} & a_{22}\cdot\mu_{E_1} + b_{22} & a_{23}\cdot\mu_{E_1} + b_{23} \\ a_{31}\cdot\mu_{E_1} + b_{31} & a_{32}\cdot\mu_{E_1} + b_{32} & a_{33}\cdot\mu_{E_1} + b_{33} \end{bmatrix}}_{[C_i^0]} + \underbrace{\begin{bmatrix} a_{11} & a_{12} & a_{13} \\ a_{21} & a_{22} & a_{23} \\ a_{31} & a_{32} & a_{33} \end{bmatrix}}_{[A_i]} \cdot \left(\sum_{m=1}^{M} \sqrt{\lambda_m} \cdot \phi_{m(\boldsymbol{x}_c^e)} \cdot z_m \right) \Rightarrow$$

$$\left[C_{i(\boldsymbol{x}_c^e,\boldsymbol{z})}\right] = \left[C_i^0\right] + \left[A_i\right] \cdot \left(\sum_{m=1}^{M} \sqrt{\lambda_m} \cdot \phi_{m(\boldsymbol{x}_c^e)} \cdot z_m \right) \quad \ldots \quad i = 1 : n_c, \tag{12}$$

where $\left[C_i^0\right]$ and $\left[A_i\right]$ are constant matrices defined as shown in Eq. (12). In other words, the stochastic effective elastic tensor tied to the θ_i candidate fiber orientation can be decomposed into the sum of a constant (mean) matrix $\left[C_i^0\right]$ and a series of M perturbation (stochastic) matrices $\left[A_i\right] \cdot \left(\sum_{m=1}^{M} \sqrt{\lambda_m} \cdot \phi_{m(\boldsymbol{x}_c^e)} \cdot z_m \right)$.

Lastly, similar to the deterministic case, the topology optimization problem is combined with the now stochastic discrete fiber orientation optimization problem by multiplying the parameterized stochastic elasticity tensor of the FE with its physical relative density. Implementing the steps outlined in Sec. (2.2), the stochastic elasticity tensor of the (e) FE for the robust TDFOOP reads as follows:

$$\left[C_{e(\tilde{x}_e,\tilde{\boldsymbol{N}}_e,\boldsymbol{z})}\right] = \tilde{x}_e^p \cdot \left(\sum_{i=1}^{n_c} \tilde{N}_{ei}^{p_n} \cdot \left[C_{i(\boldsymbol{x}_c^e,\boldsymbol{z})}\right]\right), \tag{13}$$

where now $\left[C_{i(\boldsymbol{x}_c^e,\boldsymbol{z})}\right]$ is the stochastic candidate elasticity tensor associated with the θ_i candidate fiber orientation computed at the centroid $\boldsymbol{x}_c^e$ of the FE.

3.2. SFEA by means of the Perturbation-Taylor series expansion method

The current subsection formulates the SFEA conducted at each iteration of the robust TDFOO loop, and is organized as follows: first, in Sec. (3.2.1) the stochastic stiffness matrix is derived for the (e) FE and next for the whole structural domain. Following, in Sec. (3.2.2), the SFEA is performed for the structural domain employing the first-order Taylor series expansion method.

3.2.1. Derivation of the FE's stochastic stiffness matrix

Substituting the elasticity tensor of Eq. (13) into the volume integral that computes the stiffness matrix of the FE, reads as follows:

$$\left[k_{e(\tilde{x}_e,\tilde{\boldsymbol{N}}_e,\boldsymbol{z})}\right] = \tilde{x}_e^p \cdot \left(\int_{V_E} \left[B_e\right]^T \cdot \left(\sum_{i=1}^{n_c} \tilde{N}_{ei}^{p_n} \cdot \left[C_{i(\boldsymbol{x}_c^e,\boldsymbol{z})}\right]\right) \cdot \left[B_e\right] \, dV\right) =$$

$$\tilde{x}_e^p \cdot \left(\sum_{i=1}^{n_c} \tilde{N}_{ei}^{p_n} \cdot \underbrace{\left(\int_{V_E} \left[B_e\right]^T \cdot \left[C_i^0\right] \cdot \left[B_e\right] \, dV\right)}_{\left[k_i^0\right]}\right) + \tilde{x}_e^p \cdot \left(\sum_{m=1}^{M} \sqrt{\lambda_m} \cdot \phi_{m(\boldsymbol{x}_c^e)} \cdot \left(\sum_{i=1}^{n_c} \tilde{N}_{ei}^{p_n} \cdot \underbrace{\left(\int_{V_E} \left[B_e\right]^T \cdot \left[A_i\right] \cdot \left[B_e\right] \, dV\right)}_{\left[\delta k_i\right]}\right) \cdot z_m\right)$$

$$= \underbrace{\tilde{x}_e^p \cdot \sum_{i=1}^{n_c} \tilde{N}_{ei}^{p_n} \cdot \left[k_i^0\right]}_{\left[k_{0e(\tilde{x}_e,\tilde{\boldsymbol{N}}_e)}\right]} + \underbrace{\tilde{x}_e^p \cdot \sqrt{\lambda_1} \cdot \phi_{1(\boldsymbol{x}_c^e)} \cdot \left(\sum_{i=1}^{n_c} \tilde{N}_{ei}^{p_n} \cdot \left[\delta k_i\right]\right)}_{\left[\delta k_{1e(\tilde{x}_e,\tilde{\boldsymbol{N}}_e)}\right]} \cdot z_1 + \ldots + \underbrace{\tilde{x}_e^p \cdot \sqrt{\lambda_M} \cdot \phi_{M(\boldsymbol{x}_c^e)} \cdot \left(\sum_{i=1}^{n_c} \tilde{N}_{ei}^{p_n} \cdot \left[\delta k_i\right]\right)}_{\left[\delta k_{Me(\tilde{x}_e,\tilde{\boldsymbol{N}}_e)}\right]} \cdot z_M \Rightarrow$$

$$\boxed{\left[k_{e(\tilde{x}_e,\tilde{\boldsymbol{N}}_e,\boldsymbol{z})}\right] = \left[k_{0e(\tilde{x}_e,\tilde{\boldsymbol{N}}_e)}\right] + \sum_{m=1}^{M} \left[\delta k_{me(\tilde{x}_e,\tilde{\boldsymbol{N}}_e)}\right] \cdot z_m} \tag{14}$$

where V_E is the volume of the FE, $\left[B_e\right]$ is the Jacobian matrix of the FE's shape functions, and $\left[k_{0e}\right]$ and $\left[\delta k_{me(\tilde{x}_e,\tilde{\boldsymbol{N}}e)}\right] \cdot z_m$ are the mean and the mth stochastic part of the FE's stiffness matrix, respectively. Aggregating the individual stiffness matrices of all n_e FEs inside the domain, the global stochastic stiffness matrix is expressed in the same manner as:

$$\left[K_{(\tilde{\boldsymbol{X}},\tilde{\boldsymbol{N}},\boldsymbol{z})}\right] = \left[K_{0(\tilde{\boldsymbol{X}},\tilde{\boldsymbol{N}})}\right] + \sum_{m=1}^{M} \left[\Delta K_{m(\tilde{\boldsymbol{X}},\tilde{\boldsymbol{N}})}\right] \cdot z_m \tag{15}$$

where

$$\left[K_{0(\tilde{\boldsymbol{X}},\tilde{\boldsymbol{N}})}\right] \leftarrow \biguplus_{e=1}^{n_e}\left[k_{0e(\tilde{x}_e,\tilde{\boldsymbol{N}}_e)}\right],\ \left[\Delta K_{m(\tilde{\boldsymbol{X}},\tilde{\boldsymbol{N}})}\right] \leftarrow \biguplus_{e=1}^{n_e}\left[\delta k_{me(\tilde{x}_e,\tilde{\boldsymbol{N}}_e)}\right],\ \tilde{\boldsymbol{X}} = \bigcup_{e=1}^{n_e}\tilde{x}_e \text{ and } \tilde{\boldsymbol{N}} = \bigcup_{e=1}^{n_e}\tilde{\boldsymbol{N}}_e.$$

3.2.2. Computation of the system's state variables by means of the first-order perturbation method

Perturbation methods are essentially local Taylor series expansions of the response function. In the context of static SFEA, the response function corresponds to each nodal displacement u_j inside the global displacement vector $\boldsymbol{U}_{(\tilde{\boldsymbol{X}},\tilde{\boldsymbol{N}},\boldsymbol{z})}$ and the local Taylor series is formulated around the mean of the stochastic variables. Consequently, employing a first-order Taylor series expansion for each nodal displacement around the mean $\boldsymbol{z} = \boldsymbol{0}$ of the stochastic variables, the global displacement vector is approximated as follows:

$$\boldsymbol{U}_{(\tilde{\boldsymbol{X}},\tilde{\boldsymbol{N}},\boldsymbol{z})} = \boldsymbol{U}_{0(\tilde{\boldsymbol{X}},\tilde{\boldsymbol{N}})} + \sum_{m=1}^{M}\left.\frac{d\boldsymbol{U}_{(\tilde{\boldsymbol{X}},\tilde{\boldsymbol{N}},\boldsymbol{z})}}{dz_m}\right|_{\boldsymbol{z}=\boldsymbol{0}}\cdot z_m \xRightarrow{\left.\frac{d\boldsymbol{U}}{dz_m}\right|_{\boldsymbol{z}=\boldsymbol{0}}=\boldsymbol{U}^{I}_{m(\tilde{\boldsymbol{X}},\tilde{\boldsymbol{N}})}} \boldsymbol{U}_{(\tilde{\boldsymbol{X}},\tilde{\boldsymbol{N}},\boldsymbol{z})} = \boldsymbol{U}_{0(\tilde{\boldsymbol{X}},\tilde{\boldsymbol{N}})} + \sum_{m=1}^{M}\boldsymbol{U}^{I}_{m(\tilde{\boldsymbol{X}},\tilde{\boldsymbol{N}})}\cdot z_m, \tag{16}$$

where $\boldsymbol{U}_{0(\tilde{\boldsymbol{X}},\tilde{\boldsymbol{N}})}$ is the global mean displacement vector and $\boldsymbol{U}^{I}_{m(\tilde{\boldsymbol{X}},\tilde{\boldsymbol{N}})}$ its first-order derivative vector *w.r.t.* the random variable z_m at $\boldsymbol{z} = \boldsymbol{0}$. Figure (1) illustrates the first-order perturbation method for the u_j nodal displacement at two successive iterations $n, n+1$ of the robust TDFOO loop - the figure also highlights that different states are realized for the u_j nodal displacement as the optimization progresses. At each iteration of the optimization loop, the state vectors are computed by satisfying the discrete governing equations of the physical system. For the static linear problem, these read as follows:

$$\left[K_{(\tilde{\boldsymbol{X}},\tilde{\boldsymbol{N}},\boldsymbol{z})}\right]\cdot\boldsymbol{U}_{(\tilde{\boldsymbol{X}},\tilde{\boldsymbol{N}},\boldsymbol{z})} = \boldsymbol{F}_0 \Leftrightarrow \left(\left[K_{0(\tilde{\boldsymbol{X}},\tilde{\boldsymbol{N}})}\right] + \sum_{m=1}^{M}\left[\Delta K_{m(\tilde{\boldsymbol{X}},\tilde{\boldsymbol{N}})}\right]\cdot z_m\right)\cdot\left(\boldsymbol{U}_{0(\tilde{\boldsymbol{X}},\tilde{\boldsymbol{N}})} + \sum_{m=1}^{M}\boldsymbol{U}^{I}_{m(\tilde{\boldsymbol{X}},\tilde{\boldsymbol{N}})}\cdot z_m\right) = \boldsymbol{F}_0, \tag{17}$$

where $\boldsymbol{F}_0$ is the external load vector considered in this work both deterministic and independent of the design variables. The state vectors of the system $\boldsymbol{U}_{0(\tilde{\boldsymbol{X}},\tilde{\boldsymbol{N}})}, \boldsymbol{U}^{I}_{m=1:M(\tilde{\boldsymbol{X}},\tilde{\boldsymbol{N}})}$ are computed by equating the coefficients that multiply the same z_m variable on each side of the equation, and then solving the resulting $M+1$ linear systems:

$$\bullet\ \boldsymbol{r}_{0(\tilde{\boldsymbol{X}},\tilde{\boldsymbol{N}})} : \left[K_{0(\tilde{\boldsymbol{X}},\tilde{\boldsymbol{N}})}\right]\cdot\boldsymbol{U}_{0(\tilde{\boldsymbol{X}},\tilde{\boldsymbol{N}})} - \boldsymbol{F}_0 = \boldsymbol{0} \tag{18}$$

$$\bullet\ \boldsymbol{r}_{m(\tilde{\boldsymbol{X}},\tilde{\boldsymbol{N}})} : \left[K_{0(\tilde{\boldsymbol{X}},\tilde{\boldsymbol{N}})}\right]\cdot\boldsymbol{U}^{I}_{m(\tilde{\boldsymbol{X}},\tilde{\boldsymbol{N}})} + \left[\Delta K_{m(\tilde{\boldsymbol{X}},\tilde{\boldsymbol{N}})}\right]\cdot\boldsymbol{U}_{0(\tilde{\boldsymbol{X}},\tilde{\boldsymbol{N}})} = \boldsymbol{0}\ldots\ m = 1 : M. \tag{19}$$

4. Robust TDFOO- Pt. II: Formulation of the robust TDFOOP

This section formulates the robust TDFOOP for minimization of the robust compliance function, and it is structured as follows: Sec. (4.1) formulates the expression for the robust compliance function. In Sec. (4.2), the resulting robust TDFOOP is posed and in Sec. (4.3), the sensitivities of the design functions involved in the optimization problem are analytically derived.

4.1. Formulation of the robust compliance function

When designing for robustness, the two statistical moments of the robust compliance function represent a trade-off between reward (mean) and risk (standard deviation) [37]. Therefore, the robust compliance minimization problem is typically posed as a bi-variate optimization problem seeking to minimize simultaneously the mean and the standard

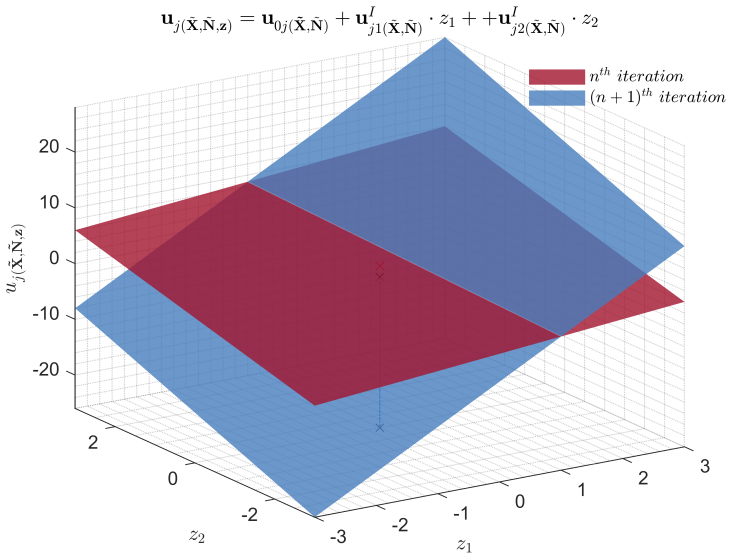

Figure 1: Following the first-order Taylor series approximation, the nodal displacement $u_{j(\tilde{\boldsymbol{X}},\tilde{\boldsymbol{N}},\boldsymbol{z})}$ of the physical system is approximated by a hyperplane about the mean of the stochastic variables. The concept is illustrated here for the case of two stochastic variables, i.e. M=2. The states are conditional on the current design point, and therefore, different states are realized between the successive iterations n and $n+1$ of the robust TDFOO loop.

deviation of the robust compliance function. The standard approach is to combine the two objectives into a single-objective function. The most popular technique for performing this conversion is the weighted sum method, whereby the single-objective function reads as:

$$\bar{f}_{(\tilde{\boldsymbol{X}},\tilde{\boldsymbol{N}})} = w_1 \cdot \mu_{f(\tilde{\boldsymbol{X}},\tilde{\boldsymbol{N}})} + w_2 \cdot \sigma_{f(\tilde{\boldsymbol{X}},\tilde{\boldsymbol{N}})}, \tag{20}$$

where $\bar{f}_{(\tilde{\boldsymbol{X}},\tilde{\boldsymbol{N}})}$ is the robust compliance function to be minimized, $\mu_{f(\tilde{\boldsymbol{X}},\tilde{\boldsymbol{N}})}$ and $\sigma_{f(\tilde{\boldsymbol{X}},\tilde{\boldsymbol{N}})}$ are the mean and standard deviation of the compliance function, respectively, and $(w_1, w_2) \in \mathbb{N}^+$ are predefined weights assigned to each one of them. The mean compliance function $\mu_{f(\tilde{\boldsymbol{X}},\tilde{\boldsymbol{N}})}$ is analyzed as follows:

$$\mu_{f(\tilde{\boldsymbol{X}},\tilde{\boldsymbol{N}})} = \mathbb{E}\left[\boldsymbol{F}_0^T \cdot \boldsymbol{U}_{(\tilde{\boldsymbol{X}},\tilde{\boldsymbol{N}},\boldsymbol{z})}\right] = \boldsymbol{F}_0^T \cdot \boldsymbol{U}_{0(\tilde{\boldsymbol{X}},\tilde{\boldsymbol{N}})}, \tag{21}$$

while the standard deviation function $\sigma_{f(\tilde{\boldsymbol{X}},\tilde{\boldsymbol{N}})}$, equals to the square root of its variance function $v_{f(\tilde{\boldsymbol{X}},\tilde{\boldsymbol{N}})}$:

$$\sigma_{f(\tilde{\boldsymbol{X}},\tilde{\boldsymbol{N}})} = \sqrt{v_{f(\tilde{\boldsymbol{X}},\tilde{\boldsymbol{N}})}} \quad \text{where} \quad v_{f(\tilde{\boldsymbol{X}},\tilde{\boldsymbol{N}})} = \mathbb{COV}_1\left[\boldsymbol{F}_0^T \cdot \boldsymbol{U}_{(\tilde{\boldsymbol{X}},\tilde{\boldsymbol{N}},\boldsymbol{z})}, \boldsymbol{F}_0^T \cdot \boldsymbol{U}_{(\tilde{\boldsymbol{X}},\tilde{\boldsymbol{N}},\boldsymbol{z})}\right], \tag{22}$$

where $\mathbb{COV}_1[\cdot,\cdot]$ is the covariance operator, and the subscript 1 indicates that the state variables are a first-order Taylor series approximation of the stochastic variables $\boldsymbol{z}$. The variance function is analyzed further as follows:

$$\begin{aligned} v_{f(\tilde{\boldsymbol{X}},\tilde{\boldsymbol{N}})} &= \boldsymbol{F}_0^T \cdot \left(\sum_{m=1}^{M}\sum_{l=1}^{M} \boldsymbol{U}^I_{m(\tilde{\boldsymbol{X}},\tilde{\boldsymbol{N}})} \cdot \left(\boldsymbol{U}^I_{l(\tilde{\boldsymbol{X}},\tilde{\boldsymbol{N}})}\right)^T \cdot \mathbb{E}\left[z_l \cdot z_m\right]\right) \cdot \boldsymbol{F}_0 \Rightarrow \\ v_{f(\tilde{\boldsymbol{X}},\tilde{\boldsymbol{N}})} &= \boldsymbol{F}_0^T \cdot \left(\sum_{m=1}^{M}\sum_{l=1}^{M} \boldsymbol{U}^T_{m(\tilde{\boldsymbol{X}},\tilde{\boldsymbol{N}})} \cdot \left(\boldsymbol{U}^I_{l(\tilde{\boldsymbol{X}},\tilde{\boldsymbol{N}})}\right)^T \cdot \delta_{lm}\right) \cdot \boldsymbol{F}_0 = \boldsymbol{F}_0^T \cdot \left(\sum_{m=1}^{M} \boldsymbol{U}^I_{m(\tilde{\boldsymbol{X}},\tilde{\boldsymbol{N}})} \cdot \left(\boldsymbol{U}^I_{m(\tilde{\boldsymbol{X}},\tilde{\boldsymbol{N}})}\right)^T\right) \cdot \boldsymbol{F}_0. \end{aligned} \tag{23}$$

As the order of magnitude of the standard deviation function is oftentimes lower than that of the mean function, the coefficients (w_1, w_2) in Eq. (20) must be tuned properly to avoid overlooking it throughout the optimization process. In this respect, normalization techniques prove to be useful in order to even out the significance between the two functions and bring them to approximately the same order of magnitude. To this end, the normalization technique proposed in [29] is adopted in this work, where the authors normalized the mean and standard deviation functions by the corresponding coordinate of the so-called utopia point in the criterion space —in the framework of multi-objective optimization, each coordinate of the utopia point in the criterion space is determined by minimizing each of the involved objectives separately—. Assuming in the present case that the coordinates of the utopia point are $\left(\mu_f^\star,\ \sigma_f^\star\right)$, each obtained by minimizing the mean and the standard deviation functions separately, the expression for the robust compliance function of Eq. (20) is modified more efficiently as follows:

$$\bar{f}_{(\tilde{\boldsymbol{X}},\tilde{\boldsymbol{N}})} = w \cdot \frac{\mu_{f(\tilde{\boldsymbol{X}},\tilde{\boldsymbol{N}})}}{\mu_f^\star} + (1-w) \cdot \frac{\sigma_{f(\tilde{\boldsymbol{X}},\tilde{\boldsymbol{N}})}}{\sigma_f^\star}, \tag{24}$$

with $w \in [0,1]$ a weight parameter. The expression in Eq. (24) is better scaled compared to that of Eq. (20) as the normalized objectives $\frac{\mu_{f(\tilde{\boldsymbol{X}},\tilde{\boldsymbol{N}})}}{\mu_f^\star}$ and $\frac{\sigma_{f(\tilde{\boldsymbol{X}},\tilde{\boldsymbol{N}})}}{\sigma_f^\star}$ range roughly in the same order of magnitude. Therefore, the robust compliance function to be minimized throughout the remainder of the paper is that of Eq. (24), nevertheless, for the sake of brevity, the initial formatting introduced in Eq. (20) is preserved, and the two weights w_1 and w_2 are set equal to $w_1 = \frac{w}{\mu_f^\star}$ and $w_2 = \frac{1-w}{\sigma_f^\star}$, respectively.

4.2. Formulation of the robust TDFOOP

Both the mean and the standard deviation functions are expressed in terms of the physical design variables $\boldsymbol{P} = \left[\tilde{\boldsymbol{X}}, \tilde{\boldsymbol{N}}\right]$, they are minimized, however, *w.r.t.* the true design variables. The robust TDFOOP for minimization of the robust compliance function is subject to: (1) the physical system's discretized governing equations constraints of Eqs. (26, 27), (2) the volume constraint of Eq. (28), (3) the self-complementary condition imposed on the penalized filtered weights of Eq. (29), and (4) the side constraints of the true design variables of Eq. (30):

Find $\left[\left(x_1,\ \boldsymbol{\xi}_1\right),\ \cdots,\ \left(x_{n_e},\ \boldsymbol{\xi}_{n_e}\right)\right]$

by solving:

$$\underset{(\tilde{\boldsymbol{X}},\tilde{\boldsymbol{N}})}{\operatorname{argmin}}\ \bar{f}_{(\tilde{\boldsymbol{X}},\tilde{\boldsymbol{N}})} = w_1 \cdot \mu_{f(\tilde{\boldsymbol{X}},\tilde{\boldsymbol{N}})} + w_2 \cdot \sigma_{f(\tilde{\boldsymbol{X}},\tilde{\boldsymbol{N}})}, \tag{25}$$

subject to:

$$\boldsymbol{r}_{0(\boldsymbol{U}_0;\tilde{\boldsymbol{X}},\tilde{\boldsymbol{N}})} : \left[K_{0(\tilde{\boldsymbol{X}},\tilde{\boldsymbol{N}})}\right] \cdot \boldsymbol{U}_{0(\tilde{\boldsymbol{X}},\tilde{\boldsymbol{N}})} - \boldsymbol{F}_0 = \boldsymbol{0}, \tag{26}$$

$$\boldsymbol{r}_{m(\boldsymbol{U}_m^I,\boldsymbol{U}_0;\tilde{\boldsymbol{X}},\tilde{\boldsymbol{N}})} : \left[K_{0(\tilde{\boldsymbol{X}},\tilde{\boldsymbol{N}})}\right] \cdot \boldsymbol{U}^I_{m(\tilde{\boldsymbol{X}},\tilde{\boldsymbol{N}})} + \left[\Delta K_{m(\tilde{\boldsymbol{X}},\tilde{\boldsymbol{N}})}\right] \cdot \boldsymbol{U}_{0(\tilde{\boldsymbol{X}},\tilde{\boldsymbol{N}})} = \boldsymbol{0} \qquad \ldots \quad m = 1 : M, \tag{27}$$

$$\frac{V_{t(\tilde{\boldsymbol{X}})}}{V_0} = f_v \Rightarrow h_{v(\tilde{\boldsymbol{X}})} : \frac{V_{t(\tilde{\boldsymbol{X}})}}{f_v \cdot V_0} - 1 = 0, \tag{28}$$

$$h_{e(\tilde{\boldsymbol{N}}_e)} : \sum_{i=1}^{n_c} \tilde{N}_{ei}^{p_n} - 1 = 0 \qquad \ldots \quad e = 1 : n_e, \tag{29}$$

$$x_{e_{\min}} \le x_e \le 1, \quad \boldsymbol{\xi}_{e_{\min}} \le \boldsymbol{\xi}_e \le \boldsymbol{\xi}_{e_{\max}} \qquad \ldots \quad e = 1 : n_e, \tag{30}$$

where $V_{t(\tilde{\boldsymbol{X}})}$ is the target volume for the structural domain corresponding to the fraction f_v of its initial V_0, and the side constraints concerning the $\boldsymbol{\xi_e}$ variables of Eq. (30) are defined as listed in Table 1 depending on the technique selected to perform the parameterization of the candidates.

To solve the above optimization problem using gradient-based solution algorithms, the first-order derivatives of all design functions are required. The procedure for analytically deriving those is detailed next.

4.3. Sensitivity analysis of the design functions

As mentioned previously, the objective is to compute the gradient of all design functions *w.r.t.* the true design variables. Starting with the true relative densities, the derivative of the robust compliance function *w.r.t.* the relative density x_e of the (e) FE reads as:

- $$\frac{d\bar{f}_{(\tilde{\boldsymbol{X}},\tilde{\boldsymbol{N}})}}{dx_e} = w_1 \cdot \frac{d\mu_{f(\tilde{\boldsymbol{X}},\tilde{\boldsymbol{N}})}}{dx_e} + w_2 \cdot \frac{d\sigma_{f(\tilde{\boldsymbol{X}},\tilde{\boldsymbol{N}})}}{dx_e}, \tag{31}$$

where the partial derivative of the mean compliance function *w.r.t.* the relative density x_e is analyzed as follows:

$$\frac{d\mu_{f(\tilde{\boldsymbol{X}},\tilde{\boldsymbol{N}})}}{dx_e} = \boldsymbol{F}_0^T \cdot \frac{d\boldsymbol{U}_{0(\tilde{\boldsymbol{X}},\tilde{\boldsymbol{N}})}}{dx_e} = \boldsymbol{F}_0^T \cdot \left(\sum_{j_e \in \mathbb{N}_e} \left[\frac{d\boldsymbol{U}_{0(\tilde{\boldsymbol{X}},\tilde{\boldsymbol{N}})}}{d\tilde{x}_{j_e}} \cdot \frac{d\tilde{x}_{j_e}}{dx_e} + \sum_{k=1}^{n_c} \frac{d\boldsymbol{U}_{0(\tilde{\boldsymbol{X}},\tilde{\boldsymbol{N}})}}{d\tilde{N}_{j_e k}} \cdot \frac{d\tilde{N}_{j_e k}}{dx_e} \right] \right) \xRightarrow{\text{Eq.(26)}: \boldsymbol{F}_0^T = \boldsymbol{U}^T_{0(\tilde{\boldsymbol{X}},\tilde{\boldsymbol{N}})} \cdot \left[K_{0(\tilde{\boldsymbol{X}},\tilde{\boldsymbol{N}})}\right]}$$

$$\boxed{\frac{d\mu_{f(\tilde{\boldsymbol{X}},\tilde{\boldsymbol{N}})}}{dx_e} = \sum_{j_e \in \mathbb{N}_e} \left[\boldsymbol{U}^T_{0(\tilde{\boldsymbol{X}},\tilde{\boldsymbol{N}})} \cdot \left[K_{0(\tilde{\boldsymbol{X}},\tilde{\boldsymbol{N}})}\right] \cdot \frac{d\boldsymbol{U}_{0(\tilde{\boldsymbol{X}},\tilde{\boldsymbol{N}})}}{d\tilde{x}_{j_e}} \cdot \frac{d\tilde{x}_{j_e}}{dx_e} + \sum_{k=1}^{n_c} \boldsymbol{U}^T_{0(\tilde{\boldsymbol{X}},\tilde{\boldsymbol{N}})} \cdot \left[K_{0(\tilde{\boldsymbol{X}},\tilde{\boldsymbol{N}})}\right] \cdot \frac{d\boldsymbol{U}_{0(\tilde{\boldsymbol{X}},\tilde{\boldsymbol{N}})}}{d\tilde{N}_{j_e k}} \cdot \frac{d\tilde{N}_{j_e k}}{dx_e} \right]} \tag{32}$$

while the same partial derivative of the standard deviation function can be expressed as follows:

$$\frac{d\sigma_{f(\tilde{\boldsymbol{X}},\tilde{\boldsymbol{N}})}}{dx_e} = \sum_{j_e \in \mathbb{N}_e} \left(\frac{d\sigma_{f(\tilde{\boldsymbol{X}},\tilde{\boldsymbol{N}})}}{d\tilde{x}_{j_e}} \cdot \frac{d\tilde{x}_{j_e}}{dx_e} + \sum_{k=1}^{n_c} \frac{d\sigma_{f(\tilde{\boldsymbol{X}},\tilde{\boldsymbol{N}})}}{d\tilde{N}_{j_e k}} \cdot \frac{d\tilde{N}_{j_e k}}{dx_e} \right) \tag{33}$$

where

$$\frac{d\sigma_{f(\tilde{\boldsymbol{X}},\tilde{\boldsymbol{N}})}}{d\tilde{x}_{j_e}} = \frac{1}{2 \cdot \sqrt{v_{f(\tilde{\boldsymbol{X}},\tilde{\boldsymbol{N}})}}} \cdot \frac{dv_{f(\tilde{\boldsymbol{X}},\tilde{\boldsymbol{N}})}}{d\tilde{x}_{j_e}} \quad \text{and} \quad \frac{d\sigma_{f(\tilde{\boldsymbol{X}},\tilde{\boldsymbol{N}})}}{d\tilde{N}_{j_e k}} = \frac{1}{2 \cdot \sqrt{v_{f(\tilde{\boldsymbol{X}},\tilde{\boldsymbol{N}})}}} \cdot \frac{dv_{f(\tilde{\boldsymbol{X}},\tilde{\boldsymbol{N}})}}{d\tilde{N}_{j_e k}}. \tag{34}$$

In Eq. (34), the derivative of the variance function *w.r.t.* the physical relative density $\tilde{x}_{j_e}$ is derived by differentiating Eq. (23):

$$\frac{dv_{f(\tilde{\boldsymbol{X}},\tilde{\boldsymbol{N}})}}{d\tilde{x}_{j_e}} = \boldsymbol{F}_0^T \cdot \left(\sum_{m=1}^{M} \frac{d\boldsymbol{U}^I_{m(\tilde{\boldsymbol{X}},\tilde{\boldsymbol{N}})}}{d\tilde{x}_{j_e}} \cdot \left(\boldsymbol{U}^I_{m(\tilde{\boldsymbol{X}},\tilde{\boldsymbol{N}})}\right)^T + \boldsymbol{U}^I_{m(\tilde{\boldsymbol{X}},\tilde{\boldsymbol{N}})} \cdot \frac{d\left(\boldsymbol{U}^I_{m(\tilde{\boldsymbol{X}},\tilde{\boldsymbol{N}})}\right)^T}{d\tilde{x}_{j_e}} \right) \cdot \boldsymbol{F}_0. \tag{35}$$

Similarly is derived its partial derivative *w.r.t.* the kth component of the $\tilde{\boldsymbol{N}}_{j_e}$ vector:

$$\frac{dv_{f(\tilde{\boldsymbol{X}},\tilde{\boldsymbol{N}})}}{d\tilde{N}_{j_e k}} = \boldsymbol{F}_0^T \cdot \left(\sum_{m=1}^{M} \frac{d\boldsymbol{U}^I_{m(\tilde{\boldsymbol{X}},\tilde{\boldsymbol{N}})}}{d\tilde{N}_{j_e k}} \cdot \left(\boldsymbol{U}^I_{m(\tilde{\boldsymbol{X}},\tilde{\boldsymbol{N}})}\right)^T + \boldsymbol{U}^I_{m(\tilde{\boldsymbol{X}},\tilde{\boldsymbol{N}})} \cdot \frac{d\left(\boldsymbol{U}^I_{m(\tilde{\boldsymbol{X}},\tilde{\boldsymbol{N}})}\right)^T}{d\tilde{N}_{j_e k}} \right) \cdot \boldsymbol{F}_0. \tag{36}$$

Finally, substituting Eqs. (34, 35, 36) in Eq. (33), the partial derivative of the standard deviation *w.r.t.* x_e is computed:

$$\boxed{\begin{aligned}\frac{d\sigma_{f(\tilde{\boldsymbol{X}},\tilde{\boldsymbol{N}})}}{dx_e} = \frac{1}{2\cdot\sqrt{v_{f(\tilde{\boldsymbol{X}},\tilde{\boldsymbol{N}})}}}\cdot\Bigg[\sum_{j_e\in\mathbb{N}_e}\boldsymbol{F}_0^T\cdot\left(\sum_{m=1}^{M}\frac{d\boldsymbol{U}^I_{m(\tilde{\boldsymbol{X}},\tilde{\boldsymbol{N}})}}{d\tilde{x}_{j_e}}\cdot\left(\boldsymbol{U}^I_{m(\tilde{\boldsymbol{X}},\tilde{\boldsymbol{N}})}\right)^T+\boldsymbol{U}^I_{m(\tilde{\boldsymbol{X}},\tilde{\boldsymbol{N}})}\cdot\frac{d\left(\boldsymbol{U}^I_{m(\tilde{\boldsymbol{X}},\tilde{\boldsymbol{N}})}\right)^T}{d\tilde{x}_{j_e}}\right)\cdot\boldsymbol{F}_0\cdot\frac{d\tilde{x}_{j_e}}{dx_e}\\ +\sum_{k=1}^{n_c}\boldsymbol{F}_0^T\cdot\left(\sum_{m=1}^{M}\frac{d\boldsymbol{U}^I_{m(\tilde{\boldsymbol{X}},\tilde{\boldsymbol{N}})}}{d\tilde{N}_{j_ek}}\cdot\left(\boldsymbol{U}^I_{m(\tilde{\boldsymbol{X}},\tilde{\boldsymbol{N}})}\right)^T+\boldsymbol{U}^I_{m(\tilde{\boldsymbol{X}},\tilde{\boldsymbol{N}})}\cdot\frac{d\left(\boldsymbol{U}^I_{m(\tilde{\boldsymbol{X}},\tilde{\boldsymbol{N}})}\right)^T}{d\tilde{N}_{j_ek}}\right)\cdot\boldsymbol{F}_0\cdot\frac{d\tilde{N}_{j_ek}}{dx_e}\Bigg].\end{aligned}} \tag{37}$$

Concerning the orientation variables, the partial derivative of the robust compliance function *w.r.t.* the lth component of the $\boldsymbol{\xi}_e$ vector reads as follows:

$$\bullet\ \frac{d\bar{f}_{(\tilde{\boldsymbol{X}},\tilde{\boldsymbol{N}})}}{d\xi_{el}} = w_1\cdot\frac{d\mu_{f(\tilde{\boldsymbol{X}},\tilde{\boldsymbol{N}})}}{d\xi_{el}} + w_2\cdot\frac{d\sigma_{f(\tilde{\boldsymbol{X}},\tilde{\boldsymbol{N}})}}{d\xi_{el}}, \tag{38}$$

where the partial derivative of the mean compliance function *w.r.t.* ξ_{el} equals to:

$$\boxed{\frac{d\mu_{f(\tilde{\boldsymbol{X}},\tilde{\boldsymbol{N}})}}{d\xi_{el}} = \boldsymbol{F}_0^T\cdot\frac{d\boldsymbol{U}_{0(\tilde{\boldsymbol{X}},\tilde{\boldsymbol{N}})}}{d\xi_{el}} = \left(\sum_{j_e\in\mathbb{N}_e}\sum_{k=1}^{n_c}\boldsymbol{U}^T_{0(\tilde{\boldsymbol{X}},\tilde{\boldsymbol{N}})}\cdot\left[K_{0(\tilde{\boldsymbol{X}},\tilde{\boldsymbol{N}})}\right]\cdot\frac{d\boldsymbol{U}_{0(\tilde{\boldsymbol{X}},\tilde{\boldsymbol{N}})}}{d\tilde{N}_{j_ek}}\cdot\frac{d\tilde{N}_{j_ek}}{d\xi_{el}}\right),} \tag{39}$$

while the partial derivative of the standard deviation function *w.r.t.* ξ_{el} equals to:

$$\boxed{\frac{d\sigma_{f(\tilde{\boldsymbol{X}},\tilde{\boldsymbol{N}})}}{d\xi_{el}} = \frac{1}{2\cdot\sqrt{v_{f(\tilde{\boldsymbol{X}},\tilde{\boldsymbol{N}})}}}\cdot\left(\sum_{j_e\in\mathbb{N}_e}\sum_{k=1}^{n_c}\boldsymbol{F}_0^T\cdot\left(\sum_{m=1}^{M}\frac{d\boldsymbol{U}^I_{m(\tilde{\boldsymbol{X}},\tilde{\boldsymbol{N}})}}{d\tilde{N}_{j_ek}}\cdot\left(\boldsymbol{U}^I_{m(\tilde{\boldsymbol{X}},\tilde{\boldsymbol{N}})}\right)^T+\boldsymbol{U}^I_{m(\tilde{\boldsymbol{X}},\tilde{\boldsymbol{N}})}\cdot\frac{d\left(\boldsymbol{U}^I_{m(\tilde{\boldsymbol{X}},\tilde{\boldsymbol{N}})}\right)^T}{d\tilde{N}_{j_ek}}\right)\cdot\boldsymbol{F}_0\cdot\frac{d\tilde{N}_{j_ek}}{d\xi_{el}}\right).} \tag{40}$$

To compute the Jacobian of the system's state vectors in Eqs. (32, 37, 39, 40), the discretized governing equations of Eqs. (26, 27) must be considered. The process for analytically deriving the Jacobian of the state vectors *w.r.t.* the physical design variables at any iteration n inside the robust TDFOO loop is detailed separately in the following subsections.

Regarding the constraint functions, the volume constraint of Eq. (28) is expanded as follows:

$$h_{v(\tilde{\boldsymbol{X}})} = \frac{V_{t(\tilde{\boldsymbol{X}})}}{f_v\cdot V_0} - 1 = \frac{v_1\cdot\tilde{x}_1+\cdots+v_{n_e}\cdot\tilde{x}_{n_e}}{f_v\cdot\left(\sum_{e=1}^{n_e}v_e\right)} - 1 = \frac{\sum_{e=1}^{n_e}v_e\cdot\tilde{x}_e}{f_v\cdot\left(\sum_{e=1}^{n_e}v_e\right)} - 1, \tag{41}$$

where v_e is the volume of the (e) FE. As such, the derivative of the volume constraint *w.r.t.* the x_e and ξ_{el} design variables, respectively, equals to:

$$\boxed{\bullet\ \frac{dh_v}{dx_e} = \sum_{j_e\in\mathbb{N}_e}\frac{dh_v}{d\tilde{x}_{j_e}}\cdot\frac{d\tilde{x}_{j_e}}{dx_e} = \frac{1}{f_v\cdot\left(\sum_{e=1}^{n_e}v_e\right)}\cdot\sum_{j_e\in\mathbb{N}_e}v_{j_e}\cdot\frac{d\tilde{x}_{j_e}}{dx_e},\qquad \bullet\ \frac{dh_v}{d\xi_{el}} = 0.} \tag{42}$$

Finally, the same partial derivatives concerning the self-complementary constraint of Eq. (29) equal to:

$$\boxed{\bullet\ \frac{dh_e}{dx_e} = 0, \qquad \bullet\ \frac{dh_e}{d\xi_{j_e l}} = p_n \cdot \left(\sum_{k=1}^{n_c} \tilde{N}_{ek}^{p_n - 1} \cdot \frac{d\tilde{N}_{ek}}{d\xi_{j_e l}} \right),} \tag{43}$$

where

$$\frac{d\tilde{N}_{ek}}{d\xi_{j_e l}} = \frac{\left(1 - \bar{d}_{j_e e}\right) \cdot \tilde{x}_{j_e}^{p}}{\sum_{j_e \in \mathbb{N}_e} \left(1 - \bar{d}_{j_e e}\right) \cdot \tilde{x}_{j_e}^{p}} \cdot \frac{dN_{j_e k}}{d\xi_{j_e l}}.$$

4.3.1. Computation of the state vectors' Jacobian

For notational brevity, the dependency of the design functions and state vectors on the physical design variables is dropped from now forth, it is maintained, however, for the stiffness matrices. Further, the index n is introduced in this section to indicate that the underscripted quantity is computed at the iteration n of the robust TDFOO loop.

Assuming that we are found at the nth design point $\boldsymbol{P}_n = \left[\tilde{\boldsymbol{X}}_n, \tilde{\boldsymbol{N}}_n\right]$ where the corresponding equilibrium constraints are being satisfied, i.e. $\boldsymbol{r}_{0(\boldsymbol{P}_n, \boldsymbol{U}_{0n})} = \boldsymbol{0}$ and $\boldsymbol{r}_{m(\boldsymbol{P}_n, \boldsymbol{U}^I_{mn}, \boldsymbol{U}_{0n})} = \boldsymbol{0}$, any perturbation $d\boldsymbol{p}$ about $\boldsymbol{P}_n$ must be accompanied by a perturbation $d\boldsymbol{U}$ in each state vector such that the respective discretized governing equation remains satisfied, as illustrated in Figure (2). Requiring the total differential of the residual equations to be zero for any perturbation about the current design point, the Jacobian of the current state vectors $\boldsymbol{U}_{0n}$ and $\boldsymbol{U}^I_{mn}$ is derived. Considering first the mean part of the governing equations, this condition is expressed mathematically as follows:

$$\bullet\ d\boldsymbol{r}_0 = \boldsymbol{r}_{0(\boldsymbol{P}_n, \boldsymbol{U}_{0n})} - \boldsymbol{r}_{0(\boldsymbol{P}_n + dp_j,\ \boldsymbol{U}_{0n} + d\boldsymbol{U}_0)} = \boldsymbol{0} \Rightarrow \left.\frac{d\boldsymbol{r}_0}{dp_j}\right|_{\boldsymbol{P}_n, \boldsymbol{U}_{0n}} \cdot dp_j + \left.\frac{d\boldsymbol{r}_0}{d\boldsymbol{U}_0}\right|_{\boldsymbol{P}_n, \boldsymbol{U}_{0n}} \cdot d\boldsymbol{U}_0 = \boldsymbol{0}, \tag{44}$$

while for the mth stochastic governing equation, the condition reads as:

$$\begin{aligned} &\bullet\ d\boldsymbol{r}_m = \boldsymbol{r}_{m(\boldsymbol{P}_n, \boldsymbol{U}_{0n}, \boldsymbol{U}^I_{mn})} - \boldsymbol{r}_{m(\boldsymbol{P}_n + dp_j,\ \boldsymbol{U}_{0n} + d\boldsymbol{U}_{0n},\ \boldsymbol{U}^I_{mn} + d\boldsymbol{U}^I_{mn})} = \boldsymbol{0} \Rightarrow \\ &\left.\frac{d\boldsymbol{r}_m}{dp_j}\right|_{\boldsymbol{P}_n, \boldsymbol{U}_{0n}, \boldsymbol{U}^I_{mn}} \cdot dp_j + \left.\frac{d\boldsymbol{r}_m}{d\boldsymbol{U}_0}\right|_{\boldsymbol{P}_n, \boldsymbol{U}_{0n}, \boldsymbol{U}^I_{mn}} \cdot d\boldsymbol{U}_0 + \left.\frac{d\boldsymbol{r}_m}{d\boldsymbol{U}^I_m}\right|_{\boldsymbol{P}_n, \boldsymbol{U}_{0n}, \boldsymbol{U}^I_{mn}} \cdot d\boldsymbol{U}^I_m = \boldsymbol{0} \quad \ldots m = 1 : M. \end{aligned} \tag{45}$$

Substituting Eq. (26) in Eq. (44) reads as follows:

$$\left.\frac{d\left[K_{0(\tilde{\boldsymbol{X}}, \tilde{\boldsymbol{N}})}\right]}{dp_j}\right|_{\boldsymbol{P}_n} \cdot \boldsymbol{U}_{0n} \cdot dp_j + \left[K_{0(\tilde{\boldsymbol{X}}_n, \tilde{\boldsymbol{N}}_n)}\right] \cdot d\boldsymbol{U}_0 = \boldsymbol{0} \Leftrightarrow \left[K_{0(\tilde{\boldsymbol{X}}_n, \tilde{\boldsymbol{N}}_n)}\right] \cdot \left.\frac{d\boldsymbol{U}_0}{dp_j}\right|_{\boldsymbol{P}_n} = -\left.\frac{d\left[K_{0(\tilde{\boldsymbol{X}}, \tilde{\boldsymbol{N}})}\right]}{dp_j}\right|_{\boldsymbol{P}_n} \cdot \boldsymbol{U}_{0n} \tag{46}$$

Similarly, substituting the mth stochastic governing in Eq. (27) equation into Eq. (45) reads as:

$$\begin{aligned} &\left.\frac{d\left[K_{0(\tilde{\boldsymbol{X}}, \tilde{\boldsymbol{N}})}\right]}{dp_j}\right|_{\boldsymbol{P}_n} \cdot \boldsymbol{U}^I_{mn} + \left.\frac{d\left[\Delta K_{m(\tilde{\boldsymbol{X}}, \tilde{\boldsymbol{N}})}\right]}{dp_j}\right|_{\boldsymbol{P}_n} \cdot \boldsymbol{U}_{0n} + \left[\Delta K_{m(\tilde{\boldsymbol{X}}_n, \tilde{\boldsymbol{N}}_n)}\right] \cdot \left.\frac{d\boldsymbol{U}_0}{dp_j}\right|_{\boldsymbol{P}_n} + \left[K_{0(\tilde{\boldsymbol{X}}_n, \tilde{\boldsymbol{N}}_n)}\right] \cdot \left.\frac{d\boldsymbol{U}^I_m}{dp_j}\right|_{\boldsymbol{P}_n} = \boldsymbol{0} \Rightarrow \\ &\left[K_{0(\tilde{\boldsymbol{X}}_n, \tilde{\boldsymbol{N}}_n)}\right] \cdot \left.\frac{d\boldsymbol{U}^I_m}{dp_j}\right|_{\boldsymbol{P}_n} = -\left(\left.\frac{d\left[K_{0(\tilde{\boldsymbol{X}}, \tilde{\boldsymbol{N}})}\right]}{dp_j}\right|_{\boldsymbol{P}_n} \cdot \boldsymbol{U}^I_{mn} + \left.\frac{d\left[\Delta K_{m(\tilde{\boldsymbol{X}}, \tilde{\boldsymbol{N}})}\right]}{dp_j}\right|_{\boldsymbol{P}_n} \cdot \boldsymbol{U}_{0n} + \left[\Delta K_{m(\tilde{\boldsymbol{X}}_n, \tilde{\boldsymbol{N}}_n)}\right] \cdot \left.\frac{d\boldsymbol{U}_0}{dp_j}\right|_{\boldsymbol{P}_n} \right) \end{aligned} \tag{47}$$

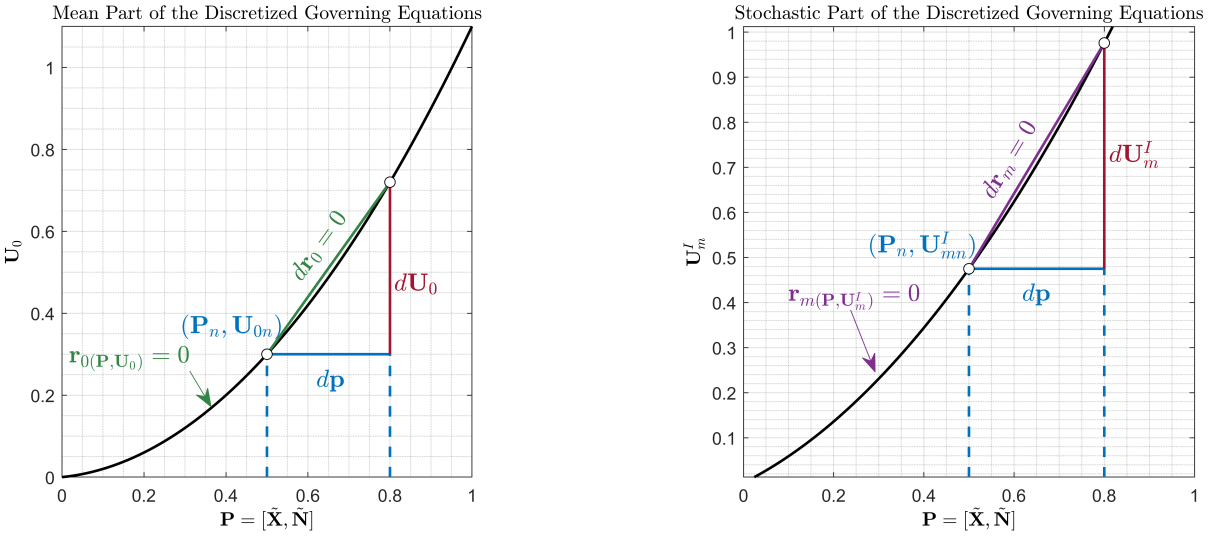

Figure 2: The appropriate differential in the state vectors $d\boldsymbol{U}_0$ and $d\boldsymbol{U}^I_{m=1:M}$ must accompany a differential of $d\boldsymbol{p}$ about the current design point $\left(\boldsymbol{P}_n, \boldsymbol{U}_{0n}, \boldsymbol{U}^I_{mn}\right)$ so that the discrete governing equations remain satisfied - moving along the contours $\boldsymbol{r}_{0(\boldsymbol{P},\boldsymbol{U}_0)} = \boldsymbol{0}$ and $\boldsymbol{r}_{m(\boldsymbol{P},\boldsymbol{U}^I_m;\boldsymbol{U}_0)} = \boldsymbol{0}$ with a step of $d\boldsymbol{p} + d\boldsymbol{U}_0$ and $d\boldsymbol{p} + d\boldsymbol{U}^I_m$, respectively.

where the index j in p_j denotes the direction of the perturbation in the physical design variables space; for instance, setting $dp_j = d\tilde{x}_{j_e}$, Eqs. (46, 47) compute the Jacobian of the state vectors $w.r.t.$ the physical relative density $\tilde{x}_{j_e}$:

- $$\left[K_{0(\tilde{\boldsymbol{X}}_n,\tilde{\boldsymbol{N}}_n)}\right] \cdot \left.\frac{d\boldsymbol{U}_0}{d\tilde{x}_{j_e}}\right|_{\boldsymbol{P}_n} = -\left.\frac{d\left[K_{0(\tilde{\boldsymbol{X}},\tilde{\boldsymbol{N}})}\right]}{d\tilde{x}_{j_e}}\right|_{\boldsymbol{P}_n} \cdot \boldsymbol{U}_{0n}, \tag{48}$$
- $$\left[K_{0(\tilde{\boldsymbol{X}}_n,\tilde{\boldsymbol{N}}_n)}\right] \cdot \left.\frac{d\boldsymbol{U}^I_m}{d\tilde{x}_{j_e}}\right|_{\boldsymbol{P}_n} = -\left(\left.\frac{d\left[K_{0(\tilde{\boldsymbol{X}},\tilde{\boldsymbol{N}})}\right]}{d\tilde{x}_{j_e}}\right|_{\boldsymbol{P}_n} \cdot \boldsymbol{U}^I_{mn} + \left.\frac{d\left[\Delta K_{m(\tilde{\boldsymbol{X}},\tilde{\boldsymbol{N}})}\right]}{d\tilde{x}_{j_e}}\right|_{\boldsymbol{P}_n} \cdot \boldsymbol{U}_{0n} + \left[\Delta K_{m(\tilde{\boldsymbol{X}}_n,\tilde{\boldsymbol{N}}_n)}\right] \cdot \left.\frac{d\boldsymbol{U}_0}{d\tilde{x}_{j_e}}\right|_{\boldsymbol{P}_n}\right), \tag{49}$$

while setting $dp_j = d\tilde{N}_{j_e k}$ compute the Jacobian of the state vectors $w.r.t.$ the kth component of the physical weight function vector $\tilde{\boldsymbol{N}}_{j_e}$:

- $$\left[K_{0(\tilde{\boldsymbol{X}}_n,\tilde{\boldsymbol{N}}_n)}\right] \cdot \left.\frac{d\boldsymbol{U}_0}{d\tilde{N}_{j_e k}}\right|_{\boldsymbol{P}_n} = -\left.\frac{d\left[K_{0(\tilde{\boldsymbol{X}},\tilde{\boldsymbol{N}})}\right]}{d\tilde{N}_{j_e k}}\right|_{\boldsymbol{P}_n} \cdot \boldsymbol{U}_{0n}, \tag{50}$$
- $$\left[K_{0(\tilde{\boldsymbol{X}}_n,\tilde{\boldsymbol{N}}_n)}\right] \cdot \left.\frac{d\boldsymbol{U}^I_m}{d\tilde{N}_{j_e k}}\right|_{\boldsymbol{P}_n} = -\left(\left.\frac{d\left[K_{0(\tilde{\boldsymbol{X}},\tilde{\boldsymbol{N}})}\right]}{d\tilde{N}_{j_e k}}\right|_{\boldsymbol{P}_n} \cdot \boldsymbol{U}^I_{mn} + \left.\frac{d\left[\Delta K_{m(\tilde{\boldsymbol{X}},\tilde{\boldsymbol{N}})}\right]}{d\tilde{N}_{j_e k}}\right|_{\boldsymbol{P}_n} \cdot \boldsymbol{U}_{0n} + \left[\Delta K_{m(\tilde{\boldsymbol{X}}_n,\tilde{\boldsymbol{N}}_n)}\right] \cdot \left.\frac{d\boldsymbol{U}_0}{d\tilde{N}_{j_e k}}\right|_{\boldsymbol{P}_n}\right). \tag{51}$$

The conditions of Eqs. (48 : 51) must be met at any iteration inside the optimization cycle, and they are being leveraged in order to compute the current gradient of the $\mu_{f(\tilde{\boldsymbol{X}},\tilde{\boldsymbol{N}})}$ and $\sigma_{f(\tilde{\boldsymbol{X}},\tilde{\boldsymbol{N}})}$ objectives at the FE level. The incorporation of these conditions into the expression derived for the gradient of the objectives in Eqs. (32, 37, 39, 40) is conducted next.

4.3.2. *Computation of the objectives functions' derivatives at the FE level*

For notational brevity, the dependency of the stiffness matrices on the physical design variables is omitted from now forth. Further, the index n is now dropped for the sake of generalizing the derivatives of the design functions for all iterations inside the optimization cycle, and last, for the sake of readability, the final expression derived for the derivatives of the mean and standard deviation functions is enclosed within boxes.

Starting with the mean compliance function, substituting the conditions of Eqs. (48, 50) in Eq. (32), the derivative of the compliance function $w.r.t.\ x_e$ is now computed at the level of its $\left(j_e\right)$ neighboring FE:

$$\frac{d\mu_f}{dx_e} = \sum_{j_e\in\mathbb{N}_e}\left[\boldsymbol{U}_0^T\cdot \underbrace{\left[K_0\right]\cdot\frac{d\boldsymbol{U}_0}{d\tilde{x}_{j_e}}}_{\text{Eq.(48)}:=-\frac{d\left[K_{0(\tilde{\boldsymbol{X}},\tilde{\boldsymbol{N}})}\right]}{d\tilde{x}_{j_e}}\cdot\boldsymbol{U}_0}\cdot\frac{d\tilde{x}_{j_e}}{dx_e} + \sum_{k=1}^{n_c}\boldsymbol{U}_0^T\cdot \underbrace{\left[K_0\right]\cdot\frac{d\boldsymbol{U}_0}{d\tilde{N}_{j_ek}}}_{\text{Eq.(50)}:=-\frac{d\left[K_{0(\tilde{\boldsymbol{X}},\tilde{\boldsymbol{N}})}\right]}{d\tilde{N}_{j_ek}}\cdot\boldsymbol{U}_0}\cdot\frac{d\tilde{N}_{j_ek}}{dx_e}\right] \Rightarrow$$

$$\frac{d\mu_f}{dx_e} = -\left(\sum_{j_e\in\mathbb{N}_e}\left[\boldsymbol{U}_0^T\cdot\frac{d\left[K_0\right]}{d\tilde{x}_{j_e}}\cdot\boldsymbol{U}_0\cdot\frac{d\tilde{x}_{j_e}}{dx_e} + \sum_{k=1}^{n_c}\boldsymbol{U}_0^T\cdot\frac{d\left[K_0\right]}{d\tilde{N}_{j_ek}}\cdot\boldsymbol{U}_0\cdot\frac{d\tilde{N}_{j_ek}}{dx_e}\right]\right) \Rightarrow$$

$$\boxed{\frac{d\mu_f}{dx_e} = -\sum_{j_e\in\mathbb{N}_e}\left(\boldsymbol{u}_{0\boldsymbol{j_e}}^T\cdot\frac{d\left[k_{0j_e}\right]}{d\tilde{x}_{j_e}}\cdot\boldsymbol{u}_{0\boldsymbol{j_e}}\right)\cdot\frac{d\tilde{x}_{j_e}}{dx_e} - \sum_{k=1}^{n_c}\sum_{j_e\in\mathbb{N}_e}\left(\boldsymbol{u}_{0\boldsymbol{j_e}}^T\cdot\frac{d\left[k_{0j_e}\right]}{d\tilde{N}_{j_ek}}\cdot\boldsymbol{u}_{0\boldsymbol{j_e}}\right)\cdot\frac{d\tilde{N}_{j_ek}}{dx_e}} \tag{52}$$

where the derivatives of the $\left(j_e\right)$ FE's mean stiffness tensor $w.r.t.$ its filtered relative density $\tilde{x}_{j_e}$ and weight function $\tilde{N}_{j_ek}$, are calculated by directly differentiating the corresponding term in Eq. (14):

$$\frac{d\left[k_{0j_e}\right]}{d\tilde{x}_{j_e}} = p\cdot\tilde{x}_{j_e}^{p-1}\cdot\left(\sum_{k=1}^{n_c}\tilde{N}_{j_ek}^{p_n}\cdot\left[k_k^0\right]\right), \qquad \frac{d\left[k_{0j_e}\right]}{d\tilde{N}_{j_ek}} = p_n\cdot\tilde{x}_{j_e}^{p}\cdot\tilde{N}_{j_ek}^{(p_n-1)}\cdot\left[k_k^0\right]. \tag{53}$$

The expression for the derivative of the standard deviation function $w.r.t.\ x_e$ is replicated here for convenience:

$$\frac{d\sigma_f}{dx_e} = \frac{1}{2\cdot\sqrt{v_f}}\cdot\left[\sum_{j_e\in\mathbb{N}_e}\left(\sum_{m=1}^{M}\boldsymbol{F}_0^T\cdot\left(\frac{d\boldsymbol{U}_m^I}{d\tilde{x}_{j_e}}\cdot\left(\boldsymbol{U}_m^I\right)^T + \boldsymbol{U}_m^I\cdot\frac{d\left(\boldsymbol{U}_m^I\right)^T}{d\tilde{x}_{j_e}}\right)\cdot\boldsymbol{F}_0\right)\cdot\frac{d\tilde{x}_{j_e}}{dx_e} + \ldots \right.$$
$$\left. \sum_{k=1}^{n_c}\left(\sum_{m=1}^{M}\boldsymbol{F}_0^T\cdot\left(\frac{d\boldsymbol{U}_m^I}{d\tilde{N}_{j_ek}}\cdot\left(\boldsymbol{U}_m^I\right)^T + \boldsymbol{U}_m^I\cdot\frac{d\left(\boldsymbol{U}_m^I\right)^T}{d\tilde{N}_{j_ek}}\right)\cdot\boldsymbol{F}_0\right)\cdot\frac{d\tilde{N}_{j_ek}}{dx_e}\right].$$

To bring the above derivative at the level of the $\left(j_e\right)$ neighboring FE, the mth term of the two nested series that compute the partial derivative of the variance function $w.r.t.\ \tilde{x}_{j_e}$ and $\tilde{N}_{j_ek}$, respectively, must be expanded; starting with the mth term of the first nested series which computes the partial derivative of the variance function $w.r.t.$ the physical relative density $\tilde{x}_{j_e}$, it is expanded as follows:

- $$\boldsymbol{F}_0^T\cdot\left(\frac{d\boldsymbol{U}_m^I}{d\tilde{x}_{j_e}}\cdot\left(\boldsymbol{U}_m^I\right)^T + \boldsymbol{U}_m^I\cdot\frac{d\left(\boldsymbol{U}_m^I\right)^T}{d\tilde{x}_{j_e}}\right)\cdot\boldsymbol{F}_0 = \boldsymbol{F}_0^T\cdot\frac{d\boldsymbol{U}_m^I}{d\tilde{x}_{j_e}}\cdot\left(\boldsymbol{U}_m^I\right)^T\cdot\boldsymbol{F}_0 + \boldsymbol{F}_0^T\cdot\boldsymbol{U}_m^I\cdot\frac{d\left(\boldsymbol{U}_m^I\right)^T}{d\tilde{x}_{j_e}}\cdot\boldsymbol{F}_0 =$$

$$2\cdot\boldsymbol{F}_0^T\cdot\frac{d\boldsymbol{U}_m^I}{d\tilde{x}_{j_e}}\cdot\left(\boldsymbol{U}_m^I\right)^T\cdot\boldsymbol{F}_0 \xRightarrow{\boldsymbol{F}_0^T=\boldsymbol{U}_0^T\cdot\left[K_0\right]} 2\cdot\boldsymbol{U}_0^T\cdot \underbrace{\left[K_0\right]\cdot\frac{d\boldsymbol{U}_m^I}{d\tilde{x}_{j_e}}}_{\text{Eq.(49)}:=-\left.\frac{d\left[K_{0(\tilde{\boldsymbol{X}},\tilde{\boldsymbol{N}})}\right]}{d\tilde{x}_{j_e}}\right|_{\boldsymbol{P}_n}\cdots}\cdot\left(\boldsymbol{U}_m^I\right)^T\cdot\left[K_0\right]\cdot\boldsymbol{U}_0 =$$

$$
\begin{aligned}
&-2\cdot\left(\boldsymbol{U}_0^T\cdot\frac{d\left[K_0\right]}{d\tilde{x}_{j_e}}\cdot\boldsymbol{U}_m^I+\boldsymbol{U}_0^T\cdot\frac{d\left[\Delta K_m\right]}{d\tilde{x}_{j_e}}\cdot\boldsymbol{U}_0+\left(\boldsymbol{U}_m^I\right)^T\cdot\frac{d\left[K_0\right]}{d\tilde{x}_{j_e}}\cdot\boldsymbol{U}_0\right)\cdot\left(\boldsymbol{U}_m^I\right)^T\cdot\left[K_0\right]\cdot\boldsymbol{U}_0=\\
&-2\cdot\left(\boldsymbol{u}_{0j_e}^T\cdot\frac{d\left[k_{0j_e}\right]}{d\tilde{x}_{j_e}}\cdot\boldsymbol{u}_{mj_e}+\boldsymbol{u}_{0j_e}^T\cdot\frac{d\left[\delta k_{mj_e}\right]}{d\tilde{x}_{j_e}}\cdot\boldsymbol{u}_{0j_e}+\boldsymbol{u}_{mj_e}^T\cdot\frac{d\left[k_{0j_e}\right]}{d\tilde{x}_{j_e}}\cdot\boldsymbol{u}_{0j_e}\right)\cdot\left(\boldsymbol{U}_m^I\right)^T\cdot\left[K_0\right]\cdot\boldsymbol{U}_0=\\
&-2\cdot\left(\boldsymbol{u}_{mj_e}^T\cdot\frac{d\left[k_{0j_e}\right]}{d\tilde{x}_{j_e}}\cdot\boldsymbol{u}_{0j_e}+\boldsymbol{u}_{0j_e}^T\cdot\frac{d\left[\delta k_{mj_e}\right]}{d\tilde{x}_{j_e}}\cdot\boldsymbol{u}_{0j_e}+\boldsymbol{u}_{0j_e}^T\cdot\frac{d\left[k_{0j_e}\right]}{d\tilde{x}_{j_e}}\cdot\boldsymbol{u}_{mj_e}\right)\cdot\left(\boldsymbol{U}_m^I\right)^T\cdot\left[K_0\right]\cdot\boldsymbol{U}_0,
\end{aligned}
\tag{54}
$$

where the partial derivatives of the $\left[\delta k_{mj_e}\right]$ perturbation matrix $w.r.t.$ $\tilde{x}_{j_e}$ and $\tilde{N}_{j_e k}$ respectively, are again derived by directly differentiating the corresponding stochastic tensor in Eq. (14):

$$
\frac{d\left[\delta k_{mj_e}\right]}{d\tilde{x}_{j_e}}=p\cdot\tilde{x}_{j_e}^{p-1}\cdot\sqrt{\lambda_m}\cdot\phi_{m(\boldsymbol{x}_c^{j_e})}\cdot\left(\sum_{k=1}^{n_c}\tilde{N}_{j_e k}^{p_n}\cdot\left[\delta k_k\right]\right),\qquad\frac{d\left[\delta k_{mj_e}\right]}{d\tilde{N}_{j_e k}}=p_n\cdot\tilde{x}_{j_e}^{p}\cdot\sqrt{\lambda_m}\cdot\phi_{m(\boldsymbol{x}_c^{j_e})}\cdot\tilde{N}_{j_e k}^{(p_n-1)}\cdot\left[\delta k_k\right].
\tag{55}
$$

Similarly, expanding the mth term of the second nested series which computes the partial derivative of the variance function $w.r.t.$ the kth component of the $\tilde{\boldsymbol{N}}_{j_e}$ weight vector reads as follows:

$$
\begin{aligned}
&\bullet\ \boldsymbol{F}_0^T\cdot\left(\frac{d\boldsymbol{U}_m^I}{d\tilde{N}_{j_e k}}\cdot\left(\boldsymbol{U}_m^I\right)^T+\boldsymbol{U}_m^I\cdot\frac{d\left(\boldsymbol{U}_m^I\right)^T}{d\tilde{N}_{j_e k}}\right)\cdot\boldsymbol{F}_0=\boldsymbol{F}_0^T\cdot\frac{d\boldsymbol{U}_m^I}{d\tilde{N}_{j_e k}}\cdot\left(\boldsymbol{U}_m^I\right)^T\cdot\boldsymbol{F}_0+\boldsymbol{F}_0^T\cdot\boldsymbol{U}_m^I\cdot\frac{d\left(\boldsymbol{U}_m^I\right)^T}{d\tilde{N}_{j_e k}}\cdot\boldsymbol{F}_0=\ldots\\
&-2\cdot\left(\boldsymbol{u}_{mj_e}^T\cdot\frac{d\left[k_{0j_e}\right]}{d\tilde{N}_{j_e k}}\cdot\boldsymbol{u}_{0j_e}+\boldsymbol{u}_{0j_e}^T\cdot\frac{d\left[\delta k_{mj_e}\right]}{d\tilde{N}_{j_e k}}\cdot\boldsymbol{u}_{0j_e}+\boldsymbol{u}_{0j_e}^T\cdot\frac{d\left[k_{0j_e}\right]}{d\tilde{N}_{j_e k}}\cdot\boldsymbol{u}_{mj_e}\right)\cdot\left(\boldsymbol{U}_m^I\right)^T\cdot\left[K_0\right]\cdot\boldsymbol{U}_0
\end{aligned}
\tag{56}
$$

Finally, substituting Eqs. (54, 56) into Eq. (37), the derivative of the standard deviation function $w.r.t.$ x_e is computed:

$$
\boxed{
\begin{aligned}
&\frac{d\sigma_f}{dx_e}=-\frac{1}{\sqrt{v_f}}\cdot\Bigg[\\
&\sum_{j_e\in\mathbb{N}_e}\left(\sum_{m=1}^{M}\left(\boldsymbol{u}_{mj_e}^T\cdot\frac{d\left[k_{0j_e}\right]}{d\tilde{x}_{j_e}}\cdot\boldsymbol{u}_{0j_e}+\boldsymbol{u}_{0j_e}^T\cdot\frac{d\left[\delta k_{mj_e}\right]}{d\tilde{x}_{j_e}}\cdot\boldsymbol{u}_{0j_e}+\boldsymbol{u}_{0j_e}^T\cdot\frac{d\left[k_{0j_e}\right]}{d\tilde{x}_{j_e}}\cdot\boldsymbol{u}_{mj_e}\right)\cdot\left(\boldsymbol{U}_m^I\right)^T\cdot\left[K_0\right]\cdot\boldsymbol{U}_0\right)\cdot\frac{d\tilde{x}_{j_e}}{dx_e}+\ldots\\
&\sum_{k=1}^{n_c}\left(\sum_{m=1}^{M}\left(\boldsymbol{u}_{mj_e}^T\cdot\frac{d\left[k_{0j_e}\right]}{d\tilde{N}_{j_e k}}\cdot\boldsymbol{u}_{0j_e}+\boldsymbol{u}_{0j_e}^T\cdot\frac{d\left[\delta k_{mj_e}\right]}{d\tilde{N}_{j_e k}}\cdot\boldsymbol{u}_{0j_e}+\boldsymbol{u}_{0j_e}^T\cdot\frac{d\left[k_{0j_e}\right]}{d\tilde{N}_{j_e k}}\cdot\boldsymbol{u}_{mj_e}\right)\cdot\left(\boldsymbol{U}_m^I\right)^T\cdot\left[K_0\right]\cdot\boldsymbol{U}_0\right)\cdot\frac{d\tilde{N}_{j_e k}}{dx_e}\Bigg]
\end{aligned}
}
\tag{57}
$$

Concerning next the derivative of the mean compliance function $w.r.t.$ the lth component of the orientation vector $\boldsymbol{\xi}_e$, it is expressed as follows:

$$\frac{d\mu_f}{d\xi_{el}} = \boldsymbol{F}_0^T \cdot \frac{d\boldsymbol{U}_0}{d\xi_{el}} = \left(\sum_{j_e \in \mathbb{N}_e} \sum_{k=1}^{n_c} \boldsymbol{U}_0^T \cdot \underbrace{\left[K_0\right] \cdot \frac{d\boldsymbol{U}_0}{d\tilde{N}_{j_e k}}}_{\text{Eq.(50)}:= -\frac{d\left[K_0\right]}{d\tilde{N}_{j_e k}} \cdot \boldsymbol{U}_0} \cdot \frac{d\tilde{N}_{j_e k}}{d\xi_{el}} \right) = -\left(\sum_{j_e \in \mathbb{N}_e} \sum_{k=1}^{n_c} \boldsymbol{U}_0^T \cdot \frac{d\left[K_0\right]}{d\tilde{N}_{j_e k}} \cdot \boldsymbol{U}_0 \cdot \frac{d\tilde{N}_{j_e k}}{d\xi_{el}} \right) \Rightarrow$$

$$\boxed{\frac{d\mu_f}{d\xi_{el}} = -\sum_{j_e \in \mathbb{N}_e} \sum_{k=1}^{n_c} \left(\boldsymbol{u}_{0j_e}^T \cdot \frac{d\left[k_{0j_e}\right]}{d\tilde{N}_{j_e k}} \cdot \boldsymbol{u}_{0j_e} \right) \cdot \frac{d\tilde{N}_{j_e k}}{d\xi_{el}}} \tag{58}$$

while that of the standard deviation function after substituting Eq. (56) in Eq. (40), reads as:

$$\boxed{\begin{aligned} &\frac{d\sigma_f}{d\xi_{el}} = -\frac{1}{\sqrt{v_f}} \cdot \\ &\left(\sum_{j_e \in \mathbb{N}_e} \sum_{k=1}^{n_c} \left(\sum_{m=1}^{M} \left(\boldsymbol{u}_{mj_e}^T \cdot \frac{d\left[k_{0j_e}\right]}{d\tilde{N}_{j_e k}} \cdot \boldsymbol{u}_{0j_e} + \boldsymbol{u}_{0j_e}^T \cdot \frac{d\left[\delta k_{mj_e}\right]}{d\tilde{N}_{j_e k}} \cdot \boldsymbol{u}_{0j_e} + \boldsymbol{u}_{0j_e}^T \cdot \frac{d\left[k_{0j_e}\right]}{d\tilde{N}_{j_e k}} \cdot \boldsymbol{u}_{mj_e} \right) \cdot \left(\boldsymbol{U}_m^I\right)^T \cdot \left[K_0\right] \cdot \boldsymbol{U}_0 \right) \cdot \frac{d\tilde{N}_{j_e k}}{d\xi_{el}} \right). \end{aligned}} \tag{59}$$

Having finally derived the analytical expression of the gradient for all design functions involved in the robust TDFOOP, gradient-based solution algorithms, such as the Method of Moving Asymptotes (MMA) [38], can be employed to solve the optimization problem in Sec. (4.2).

5. Numerical examples

In this section, the methodology is demonstrated in the academic case studies of the 2D cantilever and the half part of the Messerschmitt-Bölkow-Blohm (MBB) beam for different parameterizations of the E_1 random field. The geometric dimensions, loading, and boundary conditions of both beams are depicted in Figure (3); the cantilever beam is fixed at its left-hand side with the vertical force of 100 N being applied at its lower right tip, while the roller support conditions are applied at the left-hand side of the half MMB beam which is clamped at its lower right end, with the vertical force of 100 N being applied at its lower left tip. Both beams are subject to a discretization mesh of $[120 \times 75]$ FEs, composed of square four-node bi-linear FEs. The particular discretization mesh is considered fine enough for employing the midpoint technique to represent the random field at the centroid of the FEs.

In regards to the engineering constants of the composite lamina, the Young's Modulus along the major axis is modeled as a homogeneous RF with a mean value of $\mu_{E_1} = 200$ GPa and a standard deviation 20% of the mean, i.e., $\sigma_{E_1} = 40$ GPa. The E_2 and G_{12} moduli are both set equal to 10 GPa, while the major Poisson ratio to $v_{12} = 0.3$. It is noted that the values of the engineering constants are kept constant throughout all numerical examples.

The remainder of this section is structured as follows: to examine the effect of the spatial variability in E_1 on the robust TDFOOP, different parameterizations are examined for the RF. Sec. (5.1) specifies the parameterization instances investigated for the RF. Next, in Sec. (5.2), the design parameters of the robust TDFOOP are defined, which are kept fixed throughout all numerical examples. Lastly, Sec. (5.3) presents the robust designs predicted for the 2D cantilever and half MBB beams corresponding to the different parametrizations of the RF. In addition, for each parameterization instance of the RF, separate sub-cases are presented corresponding to different weights w being assigned to the mean and the standard deviation functions during the formulation of the robust compliance function of Eq. (24).

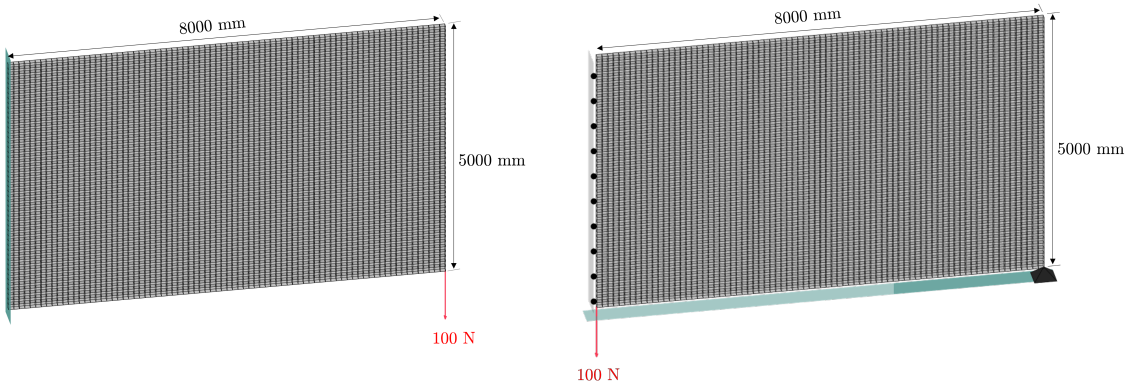

(a) 2D cantilever beam

(b) 2D half MBB beam

Figure 3: The geometry, boundary, and loading conditions of the 2D cantilever and half MBB beam case studies.

5.1. Parameterization instances considered for the RF

The heterogeneity in E_1 is modeled by means of the isotropic Gaussian kernel function, reading as follows:

$$\mathbb{COR}^{(b)}_{X_1 X_1}\left[X_{1(\boldsymbol{x}^e_c)},\ X_{1(\boldsymbol{x}^e_c+\|\delta\boldsymbol{x}\|_2)}\right] = \exp\left[-\left(\frac{\delta x_1}{b}\right)^2 - \left(\frac{\delta x_2}{b}\right)^2\right] \tag{60}$$

where $\delta x_{l=1:2} \geq 0$ is the centroidal distance of the FEs along l^{th} coordinate direction and $b \geq 0$ is the correlation length of the kernel function, considered equal for both coordinate directions. Within the framework of SFEA, it is convenient to express the parametrization of the RF in terms of the dimensionless ratio of the FE length l_e to the correlation length b, rather than solely in terms of the correlation length b. The effect of the $\frac{l_e}{b}$ ratio on the modeling and behavior of the random field is very well established from past extensive studies carried out in [39], which revealed that low ratios of $\frac{l_e}{b}$ indicate highly correlated stochastic processes and a relatively small number of terms is required in the K-L series to represent them, and conversely, that, high ratios of $\frac{l_e}{b}$ indicate less correlated stochastic processes, and thereby a large number of terms is required for their representation [40].

In the numerical examples presented in this section, the effect of the following three $\frac{l_e}{b}$ ratios is considered on the robust TDFOOP: $\frac{l_e}{b} = \{0.05,\ 0.1,\ 0.2\}$ where $l_e = 66.66$ mm in both case studies. The number of stochastic terms required in the K-L series is determined according to the following convergence metric:

$$\epsilon_M = \frac{\sum_{e=1}^{n_e}\left(\frac{\sigma^2_{E_1} - \mathbb{VAR}\left[\widehat{X}_{1(\boldsymbol{x}^e_c)}\right]}{\sigma^2_{E_1}}\right)}{n_e} \leq \tau_\epsilon, \qquad \text{where} \quad \mathbb{VAR}\left[\widehat{X}_{1(\boldsymbol{x}^e_c)}\right] = \sum_{m=1}^{M} \lambda_m \cdot \phi^2_{m(\boldsymbol{x}^e_c)}, \tag{61}$$

where ϵ_M the global relative error resulting from truncating the K-L series in M terms, $\mathbb{VAR}\left[\widehat{X}_{1(\boldsymbol{x}^e_c)}\right]$ is the approximated variance of stochastic property measured at the centroid $\boldsymbol{x}^e_c$ of the (e) FE, and τ_ϵ the prescribed truncation error tolerance. Table 2 lists the number of terms required in the K-L series for each of the three $\frac{l_e}{b}$ ratios, based on the metric of Eq. (61), for the input data of the two case studies and tolerance $\tau_\epsilon = 0.001$.

5.2. Design parameters of the robust TDFOOPs

This section lists the design parameters set for the examined robust TDFOOPs. As stated at the beginning of the section, all design parameters are held fixed throughout all numerical examples.

$\frac{l_e}{b}$	0.05	0.1	0.2
M	70	235	861

Table 2
Number of terms required in the K-L series to achieve a tolerance of $\tau_\epsilon = 0.001$ based on the metric of Eq. (61).

External penalty:	$p_n = 1$
Built-in penalty:	$p_\theta \in [0.012953, 10]$
# Candidate fiber angles per FE:	$n_c = 16$

(a) The design parameters for the NDFO-based DFOOP

Volume fraction:	$f_v = 0.3$
Penalty factor:	$p \in [1, 5]$

(b) The design parameters for the TOP

Table 3
Design parameters of the topology and morphology optimization problem

Starting with the design parameters of the TOP, the volume fraction has been set equal to $f_v = 0.3$. The initial penalty of the physical relative densities is set equal to $p = 1$ and, after the 20th iteration of the optimization loop, gradually increases within the optimization cycle until the value of $p = 5$ is reached, after which point it is held fixed.

Concerning the design parameters of the DFOOP, 16 distinct candidate fiber orientations are assigned per FE, evenly distributed within the $[-90°, 90°]$ interval. The parameterization of the resulting 16 candidate stochastic effective elasticity tensors within the FE domain is performed by employing the NDFO interpolation scheme. The penalty parameter of the physical weight functions has been set equal to $p_n = 1$. As discussed in previous works of the authors (see [35], [41]), this setting results in a trade-off between the level of discreteness in the morphology of the final design and the computational effort required to solve the optimization problem. More specifically, setting the penalty factor p_n to values greater than one leads to higher fiber convergence in the final design, i.e. to a more definitive selection of the optimal orientation among the candidates. Conversely, setting $p_n = 1$ alleviates the computational intensity of the optimization problem by automatically satisfying the self-complementary constraints in Eq. (29), at the expense, however, of obtaining lower fiber convergence levels in the final design. Thus, having set $p_n = 1$ in the current numerical examples, to attain 100% fiber convergence in the final design, the maximum component of the final filtered weight functions vector $\tilde{\boldsymbol{N}}_e^\star = \left[\tilde{N}_{e1}^\star, \dots, \tilde{N}_{en_c}^\star\right]$ is rounded to one and all other components to zero after the completion of the optimization problem. Again, even though this setting might result in rounding towards suboptimal angles in the set, it is still preferred due to its lower computational intensity.

Concerning the built-in penalty parameter p_θ of NDFO, it is initialized to the value of 10 and is gradually decreased within the optimization loop until the value of $p_\theta^{min} = 0.012953$ is reached (see [10]), at which point the optimization cycle is terminated. In other words, the optimization process concludes when 100 % fiber convergence is reached within the underlying NDFO-based DFOOP. Finally, the filter radius has been set 3 times the FE length for both the relative densities and weight functions. The design parameters for the robust TDFOOPs are summarized in Table 3.

5.3. Results

The robust designs obtained for the cantilever and half MBB beam corresponding to the different parameterizations of the RF are depicted in Figures (4:9). For all designs, the density display threshold has been set to the standard $x_d = 0.5$. Moreover, to enhance the visual clarity of the fiber orientation distribution in the figures, the fiber orientation interval $[-90°, 90°]$ has been divided into the sub-ranges $[-90°, -20°)$ $[-20°, 20°)$, and $[20°, 90°]$, and each sub-range has been assigned a distinct color. Lastly, Table 4, reports for each case study, the final values of the robust compliance function corresponding to the different parameterizations of the RF and weights w.

As depicted in the figures, the designs obtained for the cantilever and half MBB beam by minimizing solely the mean compliance function exhibit a smoother and more compact material distribution compared to those obtained by minimizing the respective robust compliance functions; these designs, however, are optimal only for the nominal value $\mu_{E_1} = 200$ GPa of the RF and sensitive to any deviations from it. It is noted at this point, that the mean compliance minimization problem has been solved only once for each case study as it remains unchanged for all three $\frac{l_e}{b}$ ratios. For convenience, however, the obtained designs are replicated in the results figures for all three ratios.

w \ $\frac{l_e}{b}$	*Cantilever Beam*			*Half MBB Beam*		
	0.05	0.1	0.2	0.05	0.1	0.2
1	1	1	1	1	1	1
0.8	1.377	1.300	1.358	1.352	1.501	1.338
0.6	1.433	1.576	1.391	1.268	2.089	1.563
0.4	1.524	1.452	1.322	1.201	1.733	1.446
0.2	1.327	1.241	1.173	0.904	1.416	1.346
0	1	1	1	1	1	1
$\left(\mu_f^\star, \sigma_f^\star\right)$	$(7.23, 0.0831)$	$(7.23, 0.0820)$	$(7.23, 0.0615)$	$(7.315, 0.0925)$	$(7.315, 0.0468)$	$(7.315, 0.0546)$

Table 4
Final values of the robust compliance function $\bar{f}$ corresponding to the different parameterizations of the RF and weight values w for the 2D cantilever and half MBB beam case studies. The last row reports the respective utopia point coordinates in mJ.

The effect of the correlation length b on the resulting topologies becomes evident when minimizing solely the standard deviation of the compliance function; that is, smaller correlation lengths b, or equivalently, less correlated stochastic processes, yield topologically finer and more intricate designs so that they can respond to local variations in the material properties and ensure robustness across different regions of the domain, whereas, higher correlation lengths yield topologically less refined designs due to the comparatively more consistent and global variation of the material property across the domain. Furthermore, the transition in the final topology for the intermediate weights seems to be relatively smooth for the $\frac{l_e}{b} = \{0.05,\ 0.1\}$ ratios and less smooth for the ratio $\frac{l_e}{b} = 0.2$, which is somewhat expected as the smoothness of those transitions is highly dependent on the complexity of the standard deviation function; increased complexity of the standard deviation function —resulting from a high number of M terms in the K-L series, and consequently number of state variables— is highly likely to cause the optimizer to get trapped in local minima that correspond to different configurations.

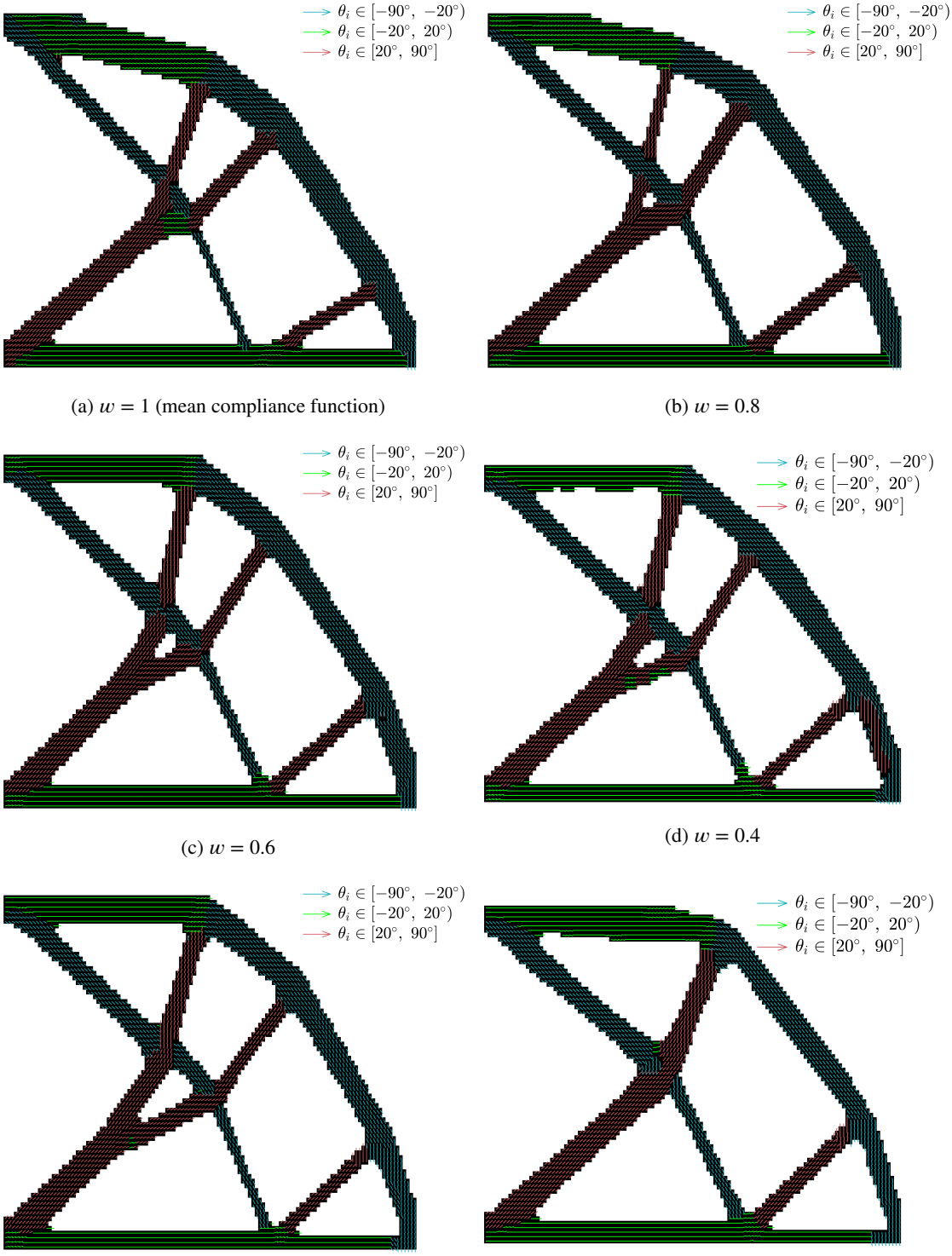

(a) $w = 1$ (mean compliance function)

(b) $w = 0.8$

(c) $w = 0.6$

(d) $w = 0.4$

(e) $w = 0.2$

(f) $w = 0$ (standard deviation of the compliance)

Figure 4: Robust designs predicted for the 2D cantilever beam for $\frac{l_e}{b} = 0.05$ and varying weights w.

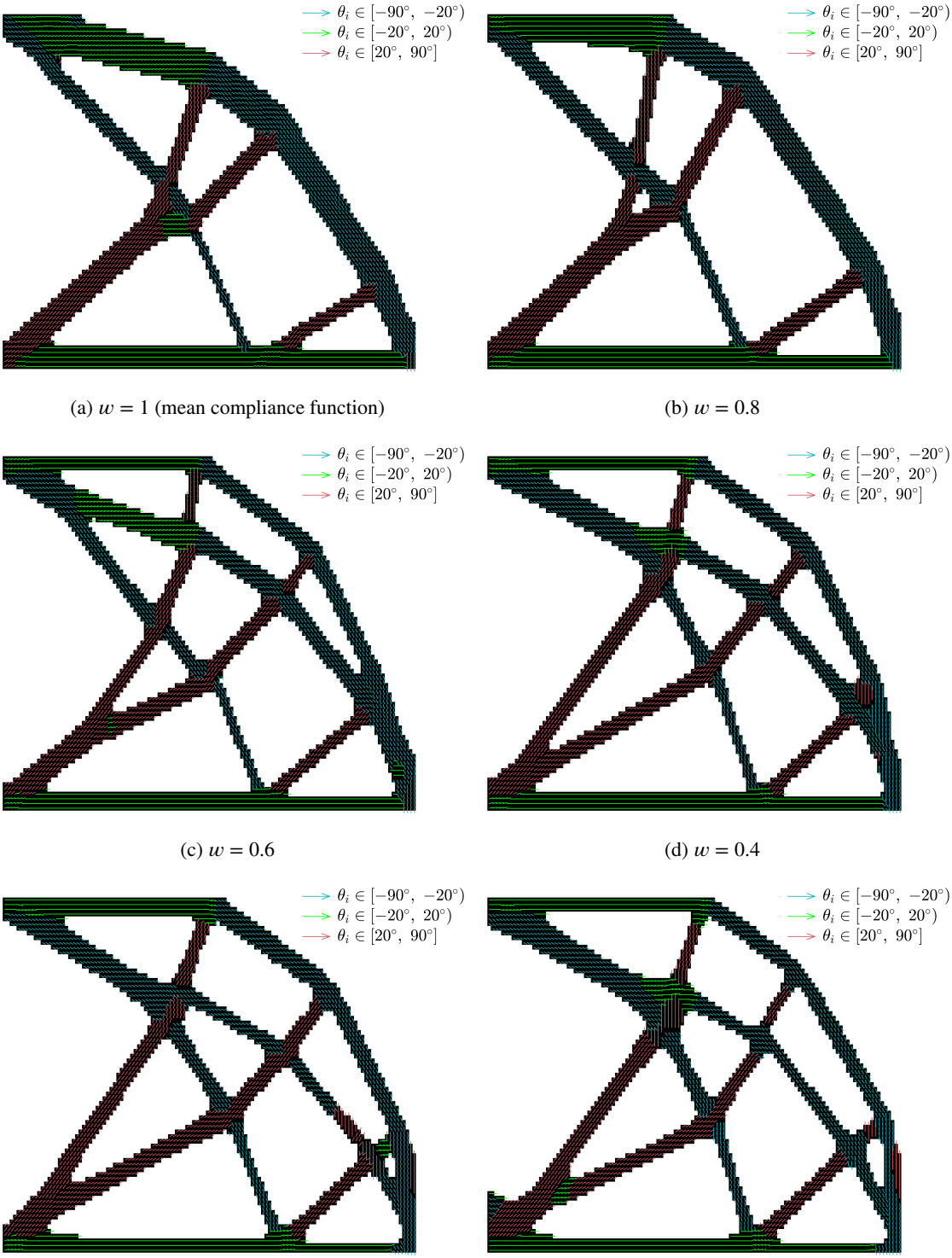

(a) $w = 1$ (mean compliance function)

(b) $w = 0.8$

(c) $w = 0.6$

(d) $w = 0.4$

(e) $w = 0.2$

(f) $w = 0$ (standard deviation of the compliance function)

Figure 5: Robust designs predicted for the 2D cantilever beam for $\frac{l_e}{b} = 0.1$ and varying weights w.

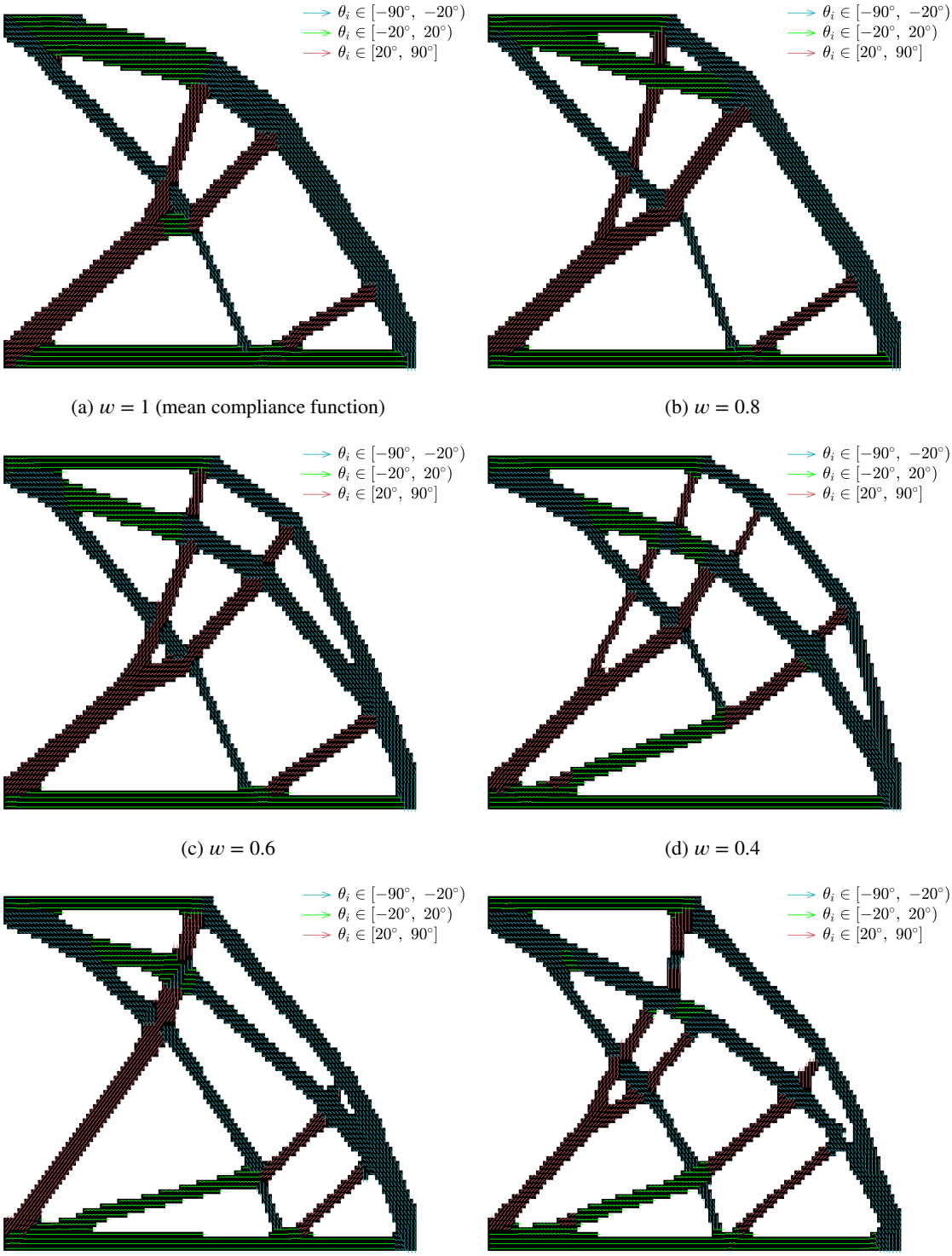

(a) $w = 1$ (mean compliance function)

(b) $w = 0.8$

(c) $w = 0.6$

(d) $w = 0.4$

(e) $w = 0.2$

(f) $w = 0$ (standard deviation of the compliance function)

Figure 6: Robust designs predicted for the 2D cantilever beam for $\frac{l_e}{b} = 0.2$ and varying weights w.

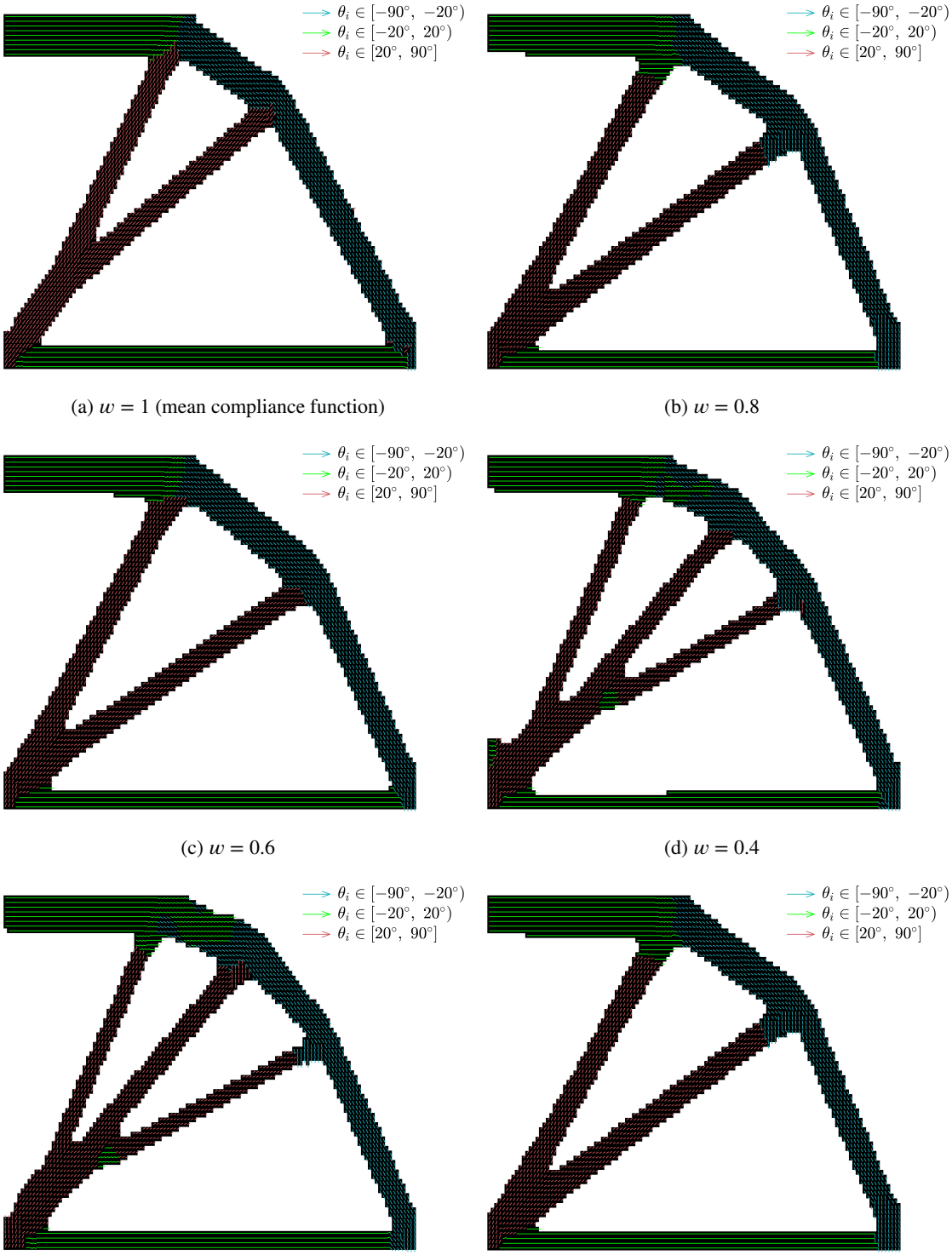

(a) $w = 1$ (mean compliance function)

(b) $w = 0.8$

(c) $w = 0.6$

(d) $w = 0.4$

(e) $w = 0.2$

(f) $w = 0$ (standard deviation of the compliance)

Figure 7: Robust designs predicted for the 2D half MBB beam for $\frac{l_e}{b} = 0.05$ and varying weights w.

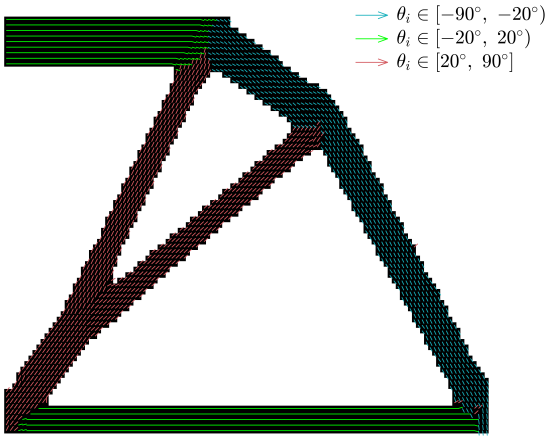

(a) $w = 1$ (mean compliance function)

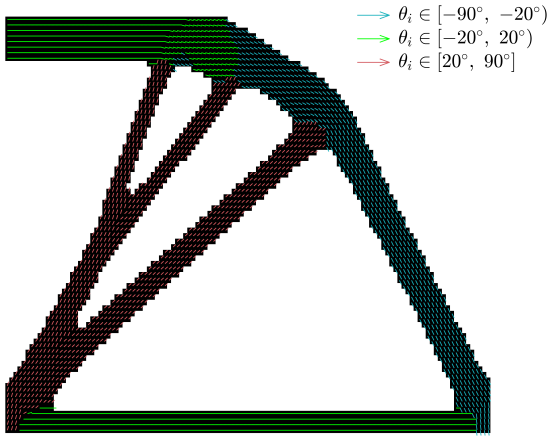

(b) $w = 0.8$

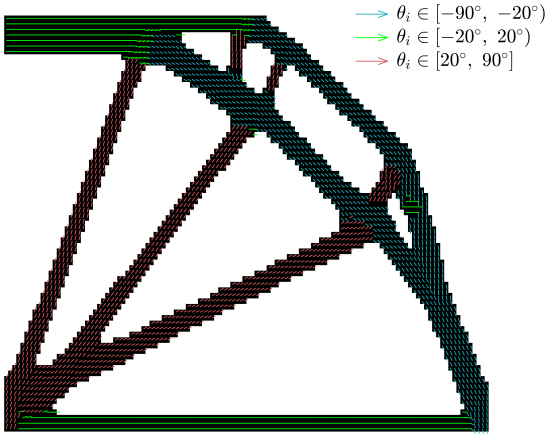

(c) $w = 0.6$

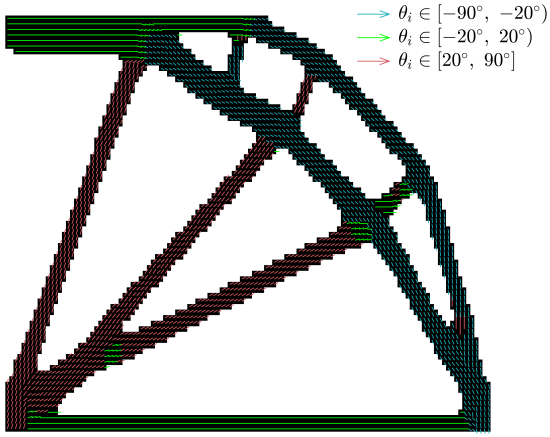

(d) $w = 0.4$

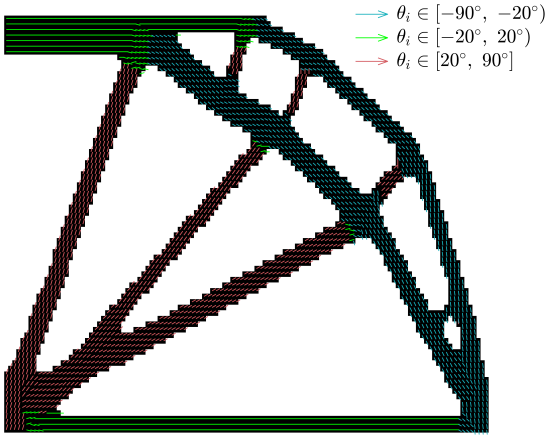

(e) $w = 0.2$

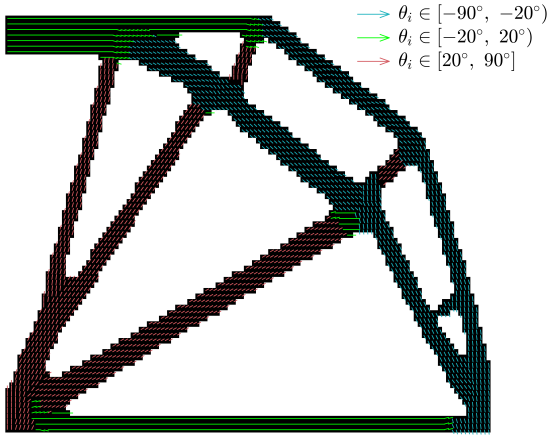

(f) $w = 0$ (standard deviation of the compliance function)

Figure 8: Robust designs predicted for the 2D half MBB beam for $\frac{l_e}{b} = 0.1$ and varying weights w.

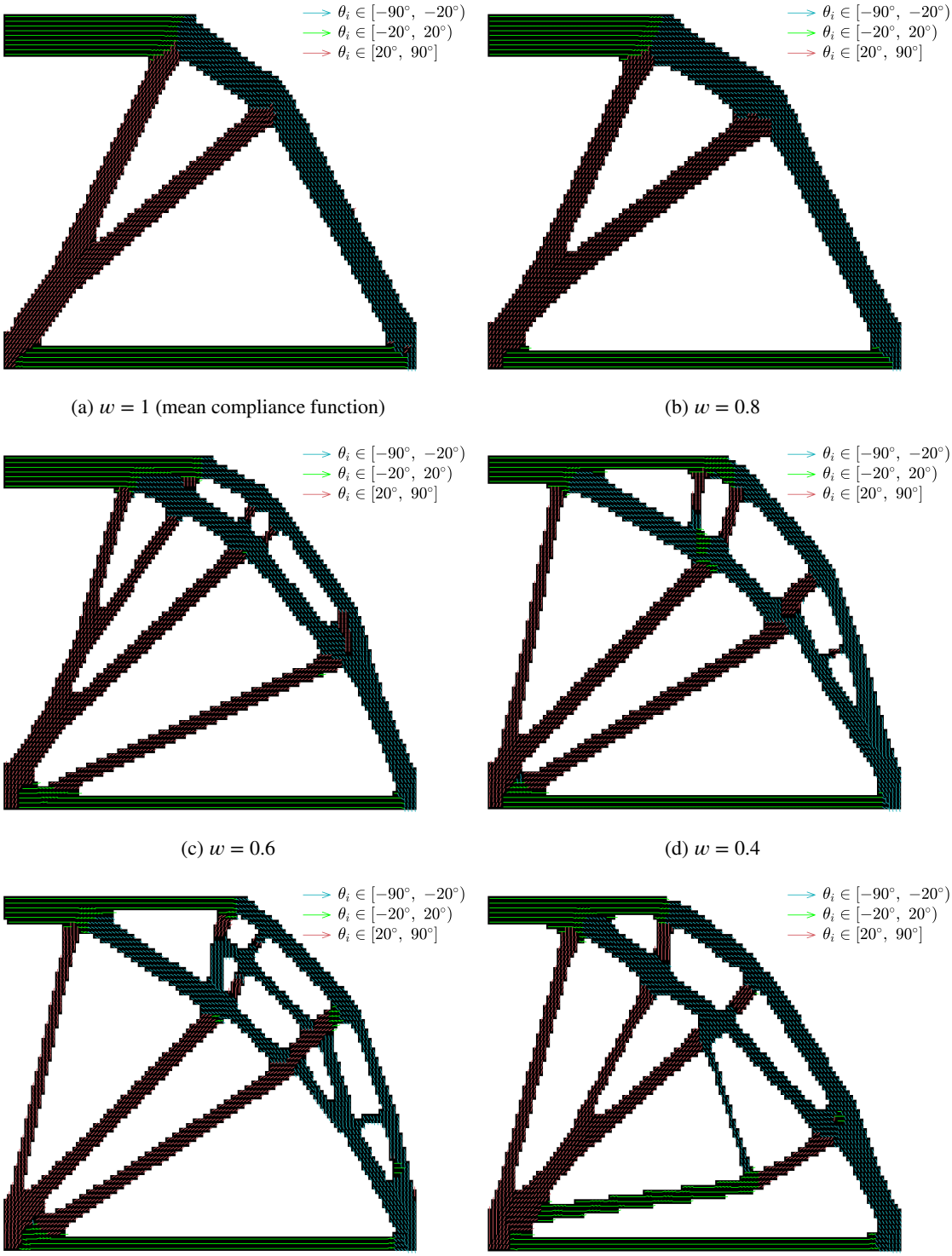

(a) $w = 1$ (mean compliance function)

(b) $w = 0.8$

(c) $w = 0.6$

(d) $w = 0.4$

(e) $w = 0.2$

(f) $w = 0$ (standard deviation of the compliance function)

Figure 9: Robust designs predicted for the 2D half MBB beam for $\frac{l_e}{b} = 0.2$ and varying weights w.

6. Extensions and recommended modifications to the methodology

The methodology can be extended/modified in some of the following ways:

- Modeling the spatial variability in the E_2 and G_{12} Moduli: The methodology has been developed and demonstrated assuming the spatial variability in the E_1 Young's Modulus of the composite lamina. By performing the same steps as for E_1, the methodology can be implemented integrally to model the spatial variability in the E_2 and G_{12} moduli as well.
- Employing more rigorous projection techniques: Throughout the development of the methodology, the penalization technique has been utilized for projecting the physical design variables toward their binary bounds. Alternatively, the Heaviside projection technique could be employed. Specifically, concerning the physical relative densities, the Heaviside projection technique has proved its superiority over the penalization technique as it ensures a 0/1 design field at the end of the optimization cycle. Similarly, the same binary result can be achieved for the weight functions when also subjected to a Heaviside-type transformation. However, in this case, the self-complementary condition of Eq. (29) is violated and must be imposed as a constraint in the optimization problem, as opposed to the special case '$p_n = 1$'of the penalization filtering technique, where the condition is automatically satisfied.
- Selecting a different interpolation technique: The interpolation scheme of NDFO was utilized in the numerical examples for the parameterization of the stochastic effective elasticity tensors as it employs a single design variable to perform the interpolation. Alternatively, any of the rest interpolation techniques listed in Table 1 can be employed for this purpose.
- Solving only the robust DFOOP: The methodology has been formulated for the concurrent topology and discrete fiber orientation optimization problem. However, it can be modified accordingly to address only the robust DFOOP. In this case, the design variables of the relative densities are excluded (i.e., are set equal to unity) from the optimization problem, leading to the formulation of the robust DFOOP solely in terms of the orientation variables:

$$\text{Find:} \quad \boldsymbol{\Xi}^{\star} = \left[\boldsymbol{\xi}_{\mathbf{1}}, \cdots, \boldsymbol{\xi}_{\boldsymbol{n}_e}\right]$$

by solving:

$$\text{argmin} \;\; \bar{f}_{(\tilde{\boldsymbol{N}})} = w_1 \cdot \mu_{f(\tilde{\boldsymbol{N}})} + w_2 \cdot \sigma_{f(\tilde{\boldsymbol{N}})},$$

subject to:

$$\bullet \; \boldsymbol{r}_{0(\boldsymbol{U}_0;\tilde{\boldsymbol{N}})} : \left[K_{0(\tilde{\boldsymbol{N}})}\right] \cdot \boldsymbol{U}_{0(\tilde{\boldsymbol{N}})} - \boldsymbol{F}_0 = \mathbf{0},$$

$$\bullet \; \boldsymbol{r}_{m(\boldsymbol{U}^I_m,\boldsymbol{U}_0;\tilde{\boldsymbol{N}})} : \left[K_{0(\tilde{\boldsymbol{N}})}\right] \cdot \boldsymbol{U}^I_{m(\tilde{\boldsymbol{N}})} + \left[\Delta K_{m(\tilde{\boldsymbol{N}})}\right] \cdot \boldsymbol{U}_{0(\tilde{\boldsymbol{N}})} = \mathbf{0} \quad \ldots \quad m = 1 : M,$$

$$\bullet \; h_{e(\tilde{\boldsymbol{N}}_e)} : \sum_{i=1}^{n_c} \tilde{N}_{ei}^{p_n} - 1 = 0 \quad \ldots \quad e = 1 : n_e,$$

$$\bullet \; \xi_{e\,min} \leq \xi_e \leq \xi_{e\,max} \quad \ldots \quad e = 1 : n_e.$$

7. Concluding remarks

The scope of this work has been to propose a methodology that incorporates the spatial variability in the engineering constants of the composite lamina into the FE-based TDFOOP for minimization of the robust compliance function. To intrusively incorporate the spatial variability into the optimization problem, the main idea involved expressing the elasticity tensor of each FE in the structural domain as the sum of a deterministic (mean) tensor and a series of stochastic (perturbation) tensors, as detailed in Sec. (3.1). To perform the nested SFEA within the optimization cycle, the methodology utilizes the first-order Taylor series expansion to approximate the system's current state variables, which limits its applicability/accuracy to linear problems with small variations. In Sec. (4), the resulting robust compliance function was formulated and the corresponding robust TDFOOP was posed. Numerical examples were conducted in Sec. (5), considering different parameterizations for the RF and weights for the mean and standard deviation functions

of the robust compliance. The effect of the correlation length on the resulting topologies was evident when minimizing solely the standard deviation of the compliance function, with smaller correlation lengths resulting in finer and more intricate final topologies that can adapt to the local variations of the material property, whereas stochastic processes of higher correlation lengths resulted in comparatively more compact final topologies. The paper concluded with some suggestions by the authors aiming to extend and improve the current mathematical and application framework of the methodology.

8. Acknowledgements

"Konstantinos-Iason Ypsilantis acknowledges the support of the Research Foundation Flanders (FWO) under the grant number 1SA8723N"

References

[1] Cheng H.C., Kikuchi N., and Ma Z.D. An improved approach for determining the optimal orientation of orthotropic material. *Structural Optimization*, 8(2-3):101 – 112, 1994.

[2] Pedersen P. On optimal orientation of orthotropic materials. *Structural Optimization*, 1(2):101 – 106, 1989.

[3] Pedersen P. Bounds on elastic energy in solids of orthotropic materials. *Structural Optimization*, 2(1):55 – 63, 1990.

[4] Pedersen P. On thickness and orientational design with orthotropic materials. *Structural Optimization*, 3(2):69 – 78, 1991.

[5] Olhoff N., Thomsen J., and Rasmussen J. Topology optimization of bi-material structures. In Pauli PEDERSEN, editor, *Optimal Design with Advanced Materials*, pages 191–206. 1993.

[6] Stegmann J. and Lund E. Discrete material optimization of general composite shell structures. *International Journal for Numerical Methods in Engineering*, 62(14):2009–2027, 2005.

[7] Bruyneel M. Sfp-a new parameterization based on shape functions for optimal material selection: application to conventional composite plies. *Structural and Multidisciplinary Optimization*, 43(1):17–27, 2011.

[8] Bruyneel M., Duysinx P., Fleury C., and Gao T. SFP: Extensions of the shape functions with penalization (sfp) parameterization for composite plies optimization. *American Institute of Aeronautics and Astronautics*, 49(10):979–1006, 2011.

[9] Gao T., Zhang W., and Duysinx P. A bi-value coding parameterization scheme for the discrete optimal orientation design of the composite laminate. *International Journal for Numerical Methods in Engineering*, 91(1):98–114, 2012.

[10] Kiyono C.Y., Silva E.C.N., and Reddy J.N. A novel fiber optimization method based on normal distribution function with continuously varying fiber path. *Composite Structures*, 160(160):503–515, January 2017.

[11] Fernandez F., Compel W. S., Lewicki J. P., and Tortorelli D. A. Optimal design of fiber reinforced composite structures and their direct ink write fabrication. *Computer Methods in Applied Mechanics and Engineering*, 353:277–307, 2019.

[12] Tian Y., Shi T., and Xia Q. A parametric level set method for the optimization of composite structures with curvilinear fibers. *Computer Methods in Applied Mechanics and Engineering*, 388:114236, 2022.

[13] Tian Y., Pu S., Zong Z., Shi T., and Xia Q. Optimization of variable stiffness laminates with gap-overlap and curvature constraints. *Composite Structures*, 230:111494, 2019.

[14] Bendsøe M. P. and Sigmund O. *Topology optimization: Theory, Methods and Applications*. Springer-Verlag, Berlin Heidelberg, 2nd edition, 2004.

[15] Zhou M. and Rozvany G. the coc algorithm, part ii: Topological, geometrical and generalized shape optimization. *Computer Methods in Applied Mechanics and Engineering*, 89:309–336, 1991.

[16] Mlejnek H. P. Some aspects of the genesis of structures. *Structural optimization*, 5, 1992.

[17] Sethian J.A. and Wiegmann A. Structural boundary design via level set and immersed interface methods. *Journal of Computational Physics*, 163(2):489–528, 2000.

[18] Osher S. J. and Santosa F. Level set methods for optimization problems involving geometry and constraints: I. frequencies of a two-density inhomogeneous drum. *Journal of Computational Physics*, 171(1):272–288, 2001.

[19] Wang M. Y., Wang X., and Guo D. A level set method for structural topology optimization. *Computer Methods in Applied Mechanics and Engineering*, 192(1):227–246, 2003.

[20] Allaire G., Jouve F., and Toader A.M. Structural optimization using sensitivity analysis and a level-set method. *Journal of Computational Physics*, 194(1):363–393, 2004.

[21] Wang Y., Li X., Long K., and Wei P. Open-source codes of topology optimization: A summary for beginners to start their research. *Computer Modeling in Engineering & Sciences*, 137(1):1–34, 2023.

[22] Nomura T., Dede E. M., Lee J., Yamasaki S., Matsumori T., Kawamoto A., and Kikuchi N. General topology optimization method with continuous and discrete orientation design using isoparametric projection. *International Journal for Numerical Methods in Engineering*, 101(8):571–605, 2015.

[23] Jiang D., Hoglund R., and Smith D. E. Continuous fiber angle topology optimization for polymer composite deposition additive manufacturing applications. *Fibers*, 7(2), 2019.

[24] Schmidt M.P., Couret L., Gout C., and Pedersen C. B. W. Structural topology optimization with smoothly varying fiber orientations. *Structural and Multidisciplinary Optimization*, 62, 2020.

[25] Guest J. K. and Igusa T. Structural optimization under uncertain loads and nodal locations. *Computer Methods in Applied Mechanics and Engineering*, 198(1):116–124, 2008.

[26] Zhao J. and Wang C. Robust structural topology optimization under random field loading uncertainty. *Structural and Multidisciplinary Optimization*, 50(3):517–522, 2014.

[27] Gao K., Do D. M., Chu S., Wu G., Kim H. A., and Featherston C. A. Robust topology optimization of structures under uncertain propagation of imprecise stochastic-based uncertain field. *Thin-Walled Structures*, 175, 2022.

[28] Lazarov B. S., Schevenels M., and Sigmund O. Topology optimization considering material and geometric uncertainties using stochastic collocation methods. *Structural and Multidisciplinary Optimization*, 46:597–612, 2012.

[29] da Silva G. A. and Cardoso E. L. Topology optimization of continuum structures subjected to uncertainties in material properties. *International Journal for Numerical Methods in Engineering*, 106(3):192–212, 2016.

[30] Yanan X., Yunkai G., Wu C., Jianguang F., and Qing L. Robust topology optimization for multiple fiber-reinforced plastic (FRP) composites under loading uncertainties. *Structural and Multidisciplinary Optimization*, 59(3):695–711, March 2019.

[31] Sheng C., Mi X., Liang G., Yan Z., and Jinhao Z. Robust topology optimization for fiber-reinforced composite structures under loading uncertainty. *Computer Methods in Applied Mechanics and Engineering*, 384, 2021.

[32] Vissarion Papadopoulos and Dimitris Giovanis. *Stochastic Finite Element Methods: An Introduction*. 01 2018.

[33] Sudret B. and Kiureghian A. *Stochastic finite element methods and reliability: a state-of-the-art report*. Department of Civil and Environmental Engineering, University of California, 2000.

[34] Wang F., Lazarov B. S., and Sigmund O. On projection methods, convergence and robust formulations in topology optimization. *Structural and Multidisciplinary Optimization*, 43(6):767 – 784, 2011.

[35] Konstantinos-Iason Ypsilantis, George Kazakis, Matthias G.R. Faes, Jan Ivens, Nikos D. Lagaros, and David Moens. A topology-based in-plane filtering technique for the combined topology and discrete fiber orientation optimization. *Computer Methods in Applied Mechanics and Engineering*, 417:116400, 2023.

[36] Armen Der Kiureghian and Jyh-Bin Ke. The stochastic finite element method in structural reliability. *Probabilistic Engineering Mechanics*, 3(2):83–91, 1988.

[37] Dunning P. D. and Kim H. A. Robust topology optimization: Minimization of expected and variance of compliance. *AIAA Journal*, 51(11):2656 – 2664, 2013.

[38] Svanberg K. The method of moving asymptotes - a new method for structural optimization. *International Journal for Numerical Methods in Engineering*, 24(2):359–373, 1987.

[39] Huang S. P., Quek S. T., and Phoon K. K. Convergence study of the truncated karhunen–loeve expansion for simulation of stochastic processes. *International Journal for Numerical Methods in Engineering*, 52(9):1029–1043, 2001.

[40] Matthias G.R. Faes, Matteo Broggi, Pol D. Spanos, and Michael Beer. Elucidating appealing features of differentiable auto-correlation functions: A study on the modified exponential kernel. *Probabilistic Engineering Mechanics*, 69:103269, July 2022.

[41] Ypsilantis K. I., Faes M., Ivens J., Lagaros N.D., and Moens D. An approach for the concurrent homogenization-based microstructure type and topology optimization problem. *Computers & Structures*, 272:106859, 2022.